

ON THE POLAR CAPS OF THE THREE MUSKETEERS¹

A. DE LUCA, P. A. CARAVEO, S. MEREGHETTI, M. NEGRONI,² AND G. F. BIGNAMI^{2,3}

Istituto di Astrofisica Spaziale e Fisica Cosmica, Sezione di Milano G. Occhialini,
CNR via Bassini 15, I-20133 Milano, Italy; deluca@mi.iasf.cnr.it

Received 2004 September 3; accepted 2004 December 27

ABSTRACT

XMM-Newton EPIC observations of PSR B0656+14, PSR B1055–52, and Geminga have substantially increased the collection of statistics available for these three isolated neutron stars, so apparently similar to deserve the nickname of the Three Musketeers, given to them by Becker & Trümper. Here we take advantage of the EPIC statistics to perform phase-resolved spectroscopy for all three objects. The phase-averaged spectrum of the Three Musketeers is best described by a three-component model. This includes two blackbody components—a cooler one, possibly originating from the bulk of the star surface, and a hotter one, coming from a smaller portion of the star surface (a “hot spot”)—plus a power law. The relative contributions of the three components are seen to vary as a function of phase, as the stars’ rotation brings into view different emitting regions. The hot spots, which have very different apparent dimensions (in spite of the similarity of the three neutron stars polar cap radii) are responsible for the bulk of the phase variation. The amplitude of the observed phase modulation is also markedly different for the three sources. Another striking aspect of our phase-resolved phenomenology is the apparent lack of any common phase alignment between the observed modulation patterns for the two blackbody components. They are seen to vary *in phase* in the case of PSR B1055–52 but *in antiphase* in the case of PSR B0656+14. These findings do not support standard and simplistic models of neutron star magnetic field configuration and surface temperature distribution.

Subject headings: pulsars: general — pulsars: individual (Geminga, PSR B0656+14, PSR B1055–52) — stars: neutron — X-rays: stars

1. INTRODUCTION

PSR B0656+14, PSR B1055–52, and Geminga are isolated neutron stars showing similar periods and period derivatives. Hence, their characteristic ages (a few 100,000 yr), their inferred magnetic fields (few 10^{12} G), and their energetics ($\dot{E}_{\text{rot}} \sim 10^{34}$ ergs s⁻¹) are very similar. Moreover, they are all nearby, making it easier to detect them at different wavelengths. Parallax distance measurements are available for Geminga (157 pc; Caraveo et al. 1996) and PSR B0656+14 (288 pc; Briskin et al. 2003), while for PSR B1055–52 the current distance estimate, based on the dispersion measure, is ~ 750 pc (Kramer et al. 2003). They shine in X-rays because of both thermal and non-thermal mechanisms. Blackbody emission from most of their surface is seen to be complemented at higher energies by power-law “tails.” They have faint optical counterparts, with a visual magnitude of $m_v \sim 25.5$ for Geminga (Bignami et al. 1987), ~ 25 for PSR B0656+14 (Caraveo et al. 1994), and ~ 24.9 for PSR B1055–52 (Mignani et al. 1997). Multicolor photometry, which is available for Geminga and PSR B0656+14, shows that their NUV magnitudes are broadly compatible with the extrapolations of their X-ray blackbody emissions, while a power-law-like excess is apparent in the optical/NIR (Mignani et al. 2004 and references therein). While PSR B1055–52 and Geminga are bona fide γ -ray pulsars (Fierro et al. 1993; Bertsch et al. 1992), for PSR B0656+14 a tentative detection awaits confirmation (Ramanamurthy et al. 1996).

Here we concentrate on the analysis of the *XMM-Newton* EPIC data collected both in imaging and timing mode. Such an exceptional harvest of X-ray photons over the ample energy interval covered by the EPIC cameras allows us to use a new tool, namely, phase resolved spectroscopy, to study the X-ray behavior of the Three Musketeers (as dubbed by Becker & Trümper 1997).

While we have already published the phase-resolved analysis of the EPIC pn data on Geminga (Caraveo et al. 2004), here we also include this source to underline similarities and differences in the phase resolved X-ray behavior of three otherwise very similar objects.

1.1. Review of the X-Ray Observations of the Three Musketeers

The EPIC data presented below come after two decades of X-ray observations of isolated neutron stars, starting with their discovery as soft, probably thermal sources by the *Einstein Observatory*.

1.1.1. Geminga

1E 0630+178 was discovered by the *Einstein* satellite while covering the γ -ray error box of the unidentified source Geminga (Bignami et al. 1983). The discovery of a common 237 ms pulsation clicked the identification, the first ever, of an unidentified γ -ray source with its X-ray counterpart (Halpern & Holt 1992; Bertsch et al. 1992). The first good-quality spectral data on Geminga were collected by *ROSAT*. Halpern & Ruderman (1993), using 7911 photons in the 0.07–1.50 keV energy band, concluded that the spectrum was well described by two blackbody curves at temperatures of 0.5×10^6 and 3×10^6 K. While the cooler component appeared to come from the full surface of the neutron star, the hotter one could have been coming from a spot covering just 3×10^{-5} of the neutron star surface,

¹ Based on observations with *XMM-Newton*, an ESA science mission with instruments and contributions directly funded by ESA member states and the US (NASA).

² Dipartimento di Fisica Nucleare e Teorica, Università degli Studi di Pavia, Via Bassi 6, I-27100 Pavia, Italy.

³ Centre d’Etude Spatiale des Rayonnements, CNRS-UPS, 9 Avenue du Colonel Roche, F-31028 Toulouse Cedex 4, France.

possibly a heated polar cap. A second, longer *ROSAT* observation, yielding 18,500 soft photons, was analyzed together with an observation by *ASCA*, providing the first 1750 “hard” (>2 keV) counts. Such a combination seemed to favor a different, composite interpretation, in which a power-law component of nonthermal emission was added to the low-temperature blackbody radiation (Halpern & Wang 1997). The power-law photon index was still poorly constrained, ranging from 2.2 to 1.5. Using a longer *ASCA* observation with 4800 photons, Jackson et al. (2002) confirmed the composite nature of Geminga’s spectrum and refined the power-law photon index value to 1.72 ± 0.1 . They tried also to perform some phase-resolved spectroscopy but could only use two phase intervals. They found the spectrum of the interval including the peak to be slightly softer than the rest of the light curve but concluded that “the difference is only marginally significant.”

1.1.2. PSR B0656+14

The definitely brighter PSR 0656+14 was first detected by the *Einstein* satellite (Cordova et al. 1989). A *ROSAT* PSPC observation allowed Finley et al. (1992) to detect the X-ray pulsation and to measure a pulsed fraction of $14\% \pm 2\%$. Further pointings were then carried out with the *ROSAT* PSPC detector in 1992 (Oegelman 1995), for a total exposure time of about 17 ks, collecting $\sim 32,000$ photons in the 0.1–2.4 keV band. The overall *ROSAT* data set was analyzed by Possenti et al. (1996), who found the bulk of the emission to be of thermal origin, well described by a blackbody curve ($T \sim 9 \times 10^5$ K) originating from a large part the star surface (emitting radius ~ 14 km assuming a distance of 760 pc, corresponding to ~ 5.3 km at the parallactic distance of 288 pc). A second spectral component was required to describe the higher energy part of the spectrum, as well as to explain a significant change of the pulse profile with energy. It was not possible, however, to discriminate between a second blackbody component ($T \sim 1.9 \times 10^6$ K) originating from a region a few hundred times smaller and a steep ($\Gamma \sim 4.5$) power law. Greiveldinger et al. (1996) coupled the *ROSAT* data set to an *ASCA* observation, which yielded ~ 2000 photons in the 0.5–10 keV band. Their best fit used a three-component model: the sum of two blackbodies (best-fit parameters very similar to the results of Possenti et al. 1996) and of a power law with photon index $\Gamma = 1.5 \pm 1.1$. More recently, PSR B0656+14 was observed with *Chandra*, both with ACIS and with the LETG. The ACIS data ($\sim 45,000$ photons in the 0.2–6 keV range) confirmed that a three-component model yields the best description of the spectrum (Pavlov et al. 2002), consistent of the sum of two blackbodies ($T_1 \sim 0.85 \times 10^6$ K, $R_1 \sim 12$ km; $T_2 \sim 1.65 \times 10^6$ K, $R_2 \sim 1$ km, using a distance of 500 pc; assuming the distance of 288 pc, $R_1 \sim 7$ km and $R_2 \sim 0.6$ km). The high spectral resolution of the gratings allowed Marshall & Schulz (2002) to exclude the presence of significant features superposed on the thermal continuum in the softer band (0.15–1 keV). The parameters of their best-fitting two-blackbody model are $T_1 \sim 0.8 \times 10^6$ K, $R_1 \sim 22.5$ km, $T_2 \sim 1.5 \times 10^6$ K, $R_2 \sim 1.7$ km, assuming a distance of 760 pc, corresponding to $R_1 \sim 8.5$ km and $R_2 \sim 650$ m at the distance of 288 pc.

1.1.3. PSR B1055–52

After the *Einstein* observatory discovery of X-ray emission from this radio pulsar (Cheng & Helfand 1983), PSR B1055–52 was observed with *ROSAT*, both with the HRI (8.6 ks yielding ~ 570 source photons) and with the PSPC (15.6 ks, for a total of ~ 5500 source photons) in 1990–1992 (Oegelman &

Finley 1993). The timing analysis unveiled the source pulsation, with a pulsed fraction increasing from $\sim 11\%$ for energies <0.5 keV to $\sim 63\%$ above 0.5 keV. The spectrum was best described by a two-component model. A blackbody with temperature of $\sim 8 \times 10^5$ K, coming from a large portion of the surface, accounts for the bulk of the X-ray emission; a second component was required, either a second, hotter ($T \sim 3.6 \times 10^6$ K) blackbody coming from an area a few $\times 10^4$ times smaller, or a steep ($\Gamma \sim 4$) power law. An *ASCA* observation could add only ~ 200 photons in the 0.5–10 keV range (Greiveldinger et al. 1996). A *Chandra* ACIS observation was taken in 2000 (42 ks exposure); results were summarized by Pavlov et al. (2002). A simultaneous fit to *Chandra* and *ROSAT* data required a three-component model, consisting of the sum of two blackbodies ($T_1 \sim 8.3 \times 10^5$ K, $R_1 \sim 12$ km, $T_2 \sim 1.6 \times 10^6$ K, $R_2 \sim 800$ m, assuming the distance to be 1 kpc; $R_1 \sim 9$ km, $R_2 \sim 600$ m at the revised distance of 750 pc) and of a power law ($\Gamma \sim 1.7$). The above authors reported the presence of a significant variation of the hot blackbody component, observed through phase-resolved spectroscopy, but they did not present detailed results. A similar three-component model has been used by Becker & Aschenbach (2002) in their analysis of *XMM-Newton* data. Spectroscopy was performed using MOS data only, which were fitted together with *ROSAT* data. Their best fit was obtained with $T_1 \sim 7.1 \times 10^5$ K, $R_1 \sim 31$ km, $T_2 \sim 1.4 \times 10^6$ K, $R_2 \sim 2.6$ km, assuming the distance to be 1 kpc (at the revised distance of 750 pc the emitting radii are $R_1 \sim 15.5$ km, $R_2 \sim 1.3$ km); the power-law photon index was found to be 1.9 ± 0.2 and the interstellar absorption $N_{\text{H}} \sim 2.3 \times 10^{20}$ cm $^{-2}$.

2. THE XMM-NEWTON EPIC DATA SETS

Geminga, PSR B0656+14, and PSR B1055–52 were observed by *XMM-Newton* as Guaranteed Time targets. The complete journal of observations is reported in Table 1. The data are now available in the *XMM-Newton* Science Archive.

While the MOS cameras (Turner et al. 2001) were operated in full-frame mode in order to image on the full field of view of the telescopes (15' radius), the pn detector (Strüder et al. 2001) was used to time-tag the photons, either in small-window mode (6 ms time resolution, imaging on a 4' \times 4' field) or in fast-timing mode (0.03 ms resolution, no spatial information along detector columns). Unfortunately, as pointed out by Becker & Aschenbach (2002), the use of the potentially promising fast-timing mode produces, as a byproduct, a background significantly higher than in small-window mode, because of the peculiar readout mode and the collapse of data along the CCD columns. Such an abnormally high background lowers the signal-to-noise ratio (S/N) above a few kilo-electron volts.

2.1. Data Reduction and Background Screening

All the data reduction was performed using the most recent release of *XMM-Newton* Science Analysis Software (SASv6.0.0). The raw observation data files (ODFs) were processed using standard pipeline tasks (*eproc* for pn, *emproc* for MOS data). We selected events with PATTERN 0–4 and PATTERN 0–12 for the pn and the MOS, respectively.

Particular care was devoted to reducing the instrumental background in the linearized event lists. First, an accurate screening for soft proton flare events was done, following the prescription of De Luca & Molendi (2004). We computed good time intervals (GTIs) setting a threshold of 3σ from the quiescent rate on the 0.5–12 keV count rate for both the pn and the MOS detectors. A more stringent threshold was adopted in the case of pn fast-timing mode observations, since the collapse

TABLE 1
JOURNAL OF *XMM-Newton* OBSERVATIONS

| Pulsar (1) | Date (2) | Obs. Time (ks) (3) | Camera (mode) ^a (4) | Good Time (s) (5) | Energy (keV) (6) | Photons (% bkg) (7) | Count Rate (8) |
|-------------------|----------------|--------------------------|-----------------------------------|-------------------------|------------------------|------------------------|-------------------|
| PSR B0656+14..... | 2001 Oct 23 | 41.0 | pn(SW) | 5970 | 0.15–8.0 | 44,600(1.7) | 7.34 ± 0.05 |
| | | | pn(Ti) | 16,850 | 0.15–2.0 | 120,000(6.3) | 6.67 ± 0.04 |
| | | | MOS1(FF) | 37,800 | 0.15–8.0 | 28,100(2.1) | 0.728 ± 0.007 |
| PSR B1055–52..... | 2000 Dec 14–15 | 81.4 | pn(Ti) | 61,900 | 0.15–6.0 | 84,450(14.4) | 1.167 ± 0.009 |
| | | | MOS1(FF) | 74,000 | 0.15–8.0 | 17,350(1.6) | 0.230 ± 0.003 |
| | | | MOS2(FF) | 74,250 | 0.15–8.0 | 18,700(1.6) | 0.247 ± 0.003 |
| Geminga..... | 2002 Apr 5 | 103.3 | pn(SW) | 55,000 | 0.15–8.0 | 52,850(5.4) | 0.909 ± 0.008 |
| | | | MOS1(FF) | 76,900 | 0.15–8.0 | 10,170(2.2) | 0.129 ± 0.002 |
| | | | MOS2(FF) | 77,400 | 0.15–8.0 | 11,300(2.4) | 0.142 ± 0.002 |

NOTES.—Col. (1): target name; col. (2): date of observation; col. (3): total time span of the observation; col. (4): detector and its readout mode; col. (5): good time of the observation; col. (6): energy range considered; col. (7): overall number of counts in the source extraction region (see § 2.2) and the fraction of background events in the specified energy range; col. (8): background-subtracted count rate.

^a SW: small-window; Ti: fast-timing; FF: full frame.

of data along the CCD readout direction increases (by a factor ~ 30) the background count rate in the source extraction region.

The pn fast-timing mode data required further cleaning. This operating mode is affected by a peculiar flaring background component (“soft flares”; see Burwitz et al. 2004), ultimately due to the interaction of charged particles (possibly heavy ions) with the CCD. Such interactions produce short (0.1–0.5 s timescale) and very intense bursts of events, with typical energies of ~ 0.22 keV for singles (monopixel events) and ~ 0.45 keV for doubles (bipixel events). To remove this background noise, which would hamper the study of the low-energy emission of our targets, ad hoc GTI files for singles and doubles were created, extracting 1 s binned light curves in the 0.2–0.3 and 0.4–0.5 keV energy ranges, respectively, and then using the same algorithm adopted for the soft proton case.

The overall GTI filter for each pn fast-timing observation was then obtained by intersecting the soft proton GTI, the soft flares GTI for singles, and the soft flares GTI for doubles. The net exposure times (after dead-time correction) for the cleaned event lists are reported in Table 1. In the case of PSR B1055–52 the observation was split between two *XMM-Newton* revolutions (186 and 187). Event lists obtained with the same instrument in the same mode in different orbits were then merged using the SAS task *merge*.

2.2. Source and Background Events Selection

To extract the source photons from the data set taken in imaging modes (full-frame for MOS and small-window for pn), we selected a circle of $45''$ radius, containing $\sim 90\%$ of the counts; in fast-timing mode we used a 17 pixel wide strip ($4''$ pixel size) containing $\sim 85\%$ of the source counts. Background photons were extracted from suitable regions on the same CCD chip containing the source: for full-frame MOS images we need an annulus of $2'$ inner radius and $4'$ outer radius; for the pn detector operated in small-window we selected two rectangular regions oriented along the CCD readout direction and covering ~ 2 arcmin²; for pn used in fast-timing mode we selected two stripes (17 and 12 pixels wide) away from the source region.

The 0.25–8.0 keV count rate observed with the MOS1 camera for PSR B0656+14 is ~ 0.9 counts s⁻¹. A modest pile-up is expected owing to the slow CCD readout in the full-frame mode (2.6 s frame time). An analysis of the event PATTERN distribu-

tion, performed with the SAS task *epatplot*, clearly showed this effect as an excess of bipixel events above 0.7 keV. To solve the problem, we simply excluded the PSF core (inner $5''$, containing about 35% of the source photons), where the pile up could be significant. No hints for pile-up in the resulting photon list was apparent in the corresponding event PATTERN distribution.

In the case of PSR B1055–52, EPIC MOS images show a faint source at an angular distance of $32''$ in the northeast direction (see Fig. 17 of Becker & Aschenbach 2002). This source has a hard spectrum (possibly a background AGN); its flux, negligible with respect to the pulsar below 2 keV, becomes comparable to the pulsar’s flux above 3 keV. To avoid possible contaminations in the study of the pulsar high-energy emission, we decided to exclude this source from the pulsar extraction region, using a $10''$ radius circle (containing $\sim 60\%$ of the counts at 5 keV) as a geometrical mask. A comparable selection was not possible in pn timing mode, since along the RAWX direction (perpendicular to the readout direction), where spatial information is maintained, the angular separation of the two sources is < 4 pixels. Therefore, the flux measured by the pn in excess of ~ 3 keV may be contaminated by some contribution from such background source, and its absolute value should be taken with caution.

Background-subtracted count rates for the three neutron stars are reported in Table 1, together with the number of collected photons.

3. EPIC DATA ANALYSIS

With a number of time-tagged photons (see Table 1) that more than doubles all previous statistics, EPIC now offers the first chance of meaningful phase-resolved spectroscopy for the Three Musketeers. Following the procedure outlined by Caraveo et al. (2004), in this paper we

1. address the phase-averaged spectral shape of the three objects to obtain useful pieces of information on the components needed to fit their overall spectra;
2. perform the timing analysis to search for the best period and to perform the phase alignment;
3. divide the folded light curves in 10 phase intervals and extract the spectra corresponding to each phase interval; and
4. fit each spectrum using the same components found to best describe the integrated spectrum and compute the corresponding phase-resolved spectral parameters.

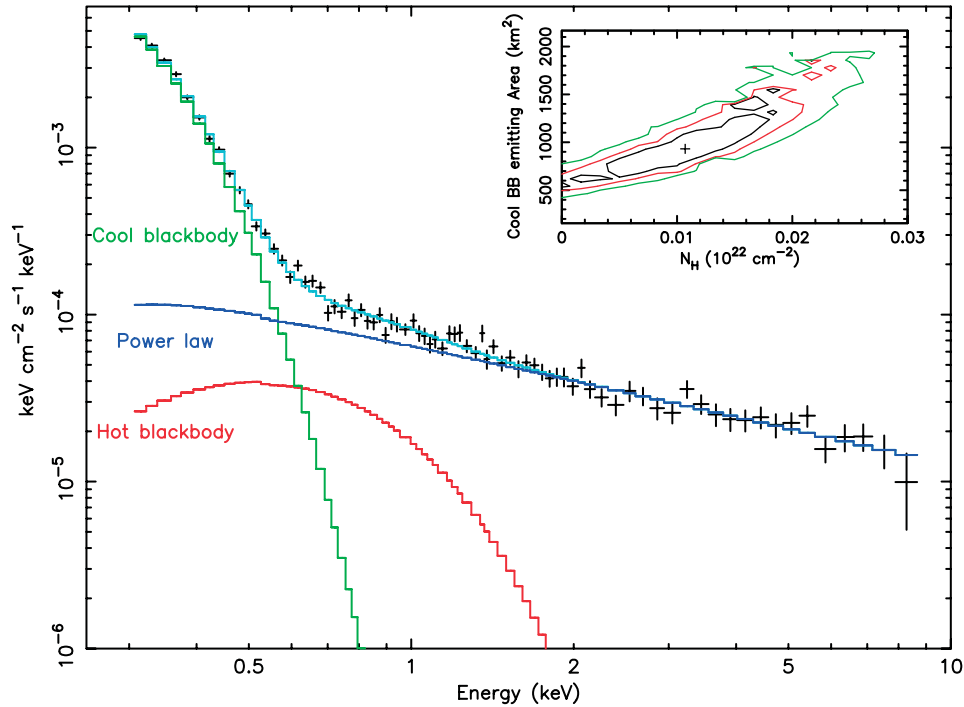


FIG. 1.—Unfolded phase-integrated spectrum of Geminga. Only data from the pn camera are plotted. This figure is adapted from Caraveo et al. (2004); a different color code is used here (see also Figs. 2 and 3). The best-fitting spectral model is represented by the light blue line. As discussed in the text, this is obtained by the sum of a cool blackbody component (green), a hot blackbody component (red), and a power law (blue). Detailed values of the best-fitting parameters are reported in Table 2. The inset shows confidence contours for the interstellar column density N_{H} vs. the emitting surface for the cool blackbody. The 68%, 90%, and 99% confidence levels for two parameters of interest are plotted. Caraveo et al. (2004) fixed the N_{H} value to $1.07 \times 10^{20} \text{ cm}^{-2}$ (resulting from *ROSAT* data) to obtain their set of best-fitting parameters (see Table 2).

In the following section we discuss in detail each step for the cases of PSR B0656+14 and PSR B1055–52. The case of Geminga was described by Caraveo et al. (2004); here we report the results to facilitate a synoptic view of the phenomenology of the Three Musketeers.

3.1. Phase-integrated Spectral Analysis

Spectra for the source and background events, extracted using the regions described in § 2.2, were rebinned in order to have at least 40 counts channel^{-1} . We added a 5% systematic error to each spectral bin to account for calibration uncertainties among different instruments/modes. Ad hoc redistribution matrices and effective area files were generated using the *rmfgen* and *arfgen* tasks of SAS. The spectral analysis was performed with XSPEC v11.2. We selected 0.25 keV as the lower bound for the spectral study, since below this energy the calibration is still uncertain; the upper bound was selected on the basis of the observed S/N, which depends both on the sources' spectra and on the operating mode used. As discussed in § 2.1, the spectra collected by the pn in fast-timing mode suffer from a rather high background, which hampers the study of our targets at high energy, at which such sources are rather faint. For PSR B0656+14 spectra obtained in fast-timing mode turned out to be useful up to 2 keV, while for PSR B1055–52 we could include data up to 6 keV. Spectra from MOS1/2 in full-frame mode, as well as from the pn small-window mode, were used up to 8 keV. MOS and pn spectra were fitted simultaneously, leaving a cross-normalization factor as the only free parameter.

No significant spectral features are detected superposed on the continuum of the Three Musketeers, either in emission or in absorption. As in the case of Geminga (Caraveo et al. 2004) (Fig. 1), the best-fitting model is found by combining two

blackbody curves and a power law. This confirms the findings made by Pavlov et al. (2002), based on *Chandra* observations of PSR B0656+14 and PSR B1055–52, and by Becker & Aschenbach (2002), who analyzed *XMM-Newton* (MOS only) data for PSR B1055–52. Using the best-fitting parameters reported in Table 2, we obtain $\chi^2_{\nu} = 1.1$ (368 degrees of freedom [dof]) for PSR B0656+14 (Fig. 2) and $\chi^2_{\nu} = 1.0$ (327 dof) for PSR B1055–52 (Fig. 3). The use of a second power law instead of the hotter blackbody yields photon indices of ~ 6.5 for PSR B0656+14 and ~ 5.6 for PSR B1055–52 while lowering the fit quality ($\chi^2_{\nu} > 1.5$ and $\chi^2_{\nu} > 1.1$ for the two cases, respectively). We note that a single-temperature, magnetized neutron star atmosphere model (Zavlin et al. 1996) cannot adequately reproduce the profile of the low-energy part of the spectrum of PSR B0656+14 and PSR B1055–52, similarly to the case of a single-blackbody curve. Moreover, this model requires a very large emitting surface (with emitting radii of ~ 100 km—this is true also for Geminga). Therefore, this model cannot provide a satisfactory description of the spectra of the Three Musketeers.

A synoptic plot of the spectra of the Three Musketeers is shown in Figure 4. It is easy to note the definitely higher S/N in the high-energy portion (> 2 keV) of the spectrum of Geminga, in spite of a flux only slightly higher in this energy range. This is mainly due to the different operating modes used for the pn detector in the observations of the three targets, especially to the much lower background in the pn small-window mode with respect to fast-timing mode. The power-law component in the spectra of PSR B0656+14 and PSR B1055–52 is constrained by the MOS spectra and (in the case of PSR B0656+14) by the short pn small-window observation (see the legend of Fig. 4 for further details). We summarize the results of the EPIC spectral fits for the Three Musketeers in Table 2, in which errors are

TABLE 2
RESULTS OF PHASE-INTEGRATED SPECTROSCOPY

| Parameter | PSR B0656+14 | PSR B1055–52 | Geminga ^a |
|--|------------------------------------|------------------------------------|------------------------------|
| N_{H} (10^{20} cm^{-2})..... | 4.3 ± 0.2 | 2.7 ± 0.2 | 1.07 (fixed) |
| kT_{CBB} (K)..... | $(6.5 \pm 0.1) \times 10^5$ | $(7.9 \pm 0.3) \times 10^5$ | $(5.0 \pm 0.1) \times 10^5$ |
| R_{CBB} (km)..... | $20.9^{+2.7}_{-3.8}$ | $12.3^{+1.5}_{-0.7}$ | 8.6 ± 1.0 |
| kT_{HBB} (K)..... | $(1.25 \pm 0.03) \times 10^6$ | $(1.79 \pm 0.06) \times 10^6$ | $(1.9 \pm 0.3) \times 10^6$ |
| R_{HBB} (m)..... | 1800 ± 150 | 460 ± 60 | 40 ± 10 |
| Γ | 2.1 ± 0.3 | 1.7 ± 0.1 | 1.7 ± 0.1 |
| I_{PL} ($\text{ph cm}^{-2} \text{ s}^{-1} \text{ keV}^{-1}$ at 1 keV)..... | $4.3^{+0.6}_{-1.5} \times 10^{-5}$ | $1.9^{+0.3}_{-0.2} \times 10^{-5}$ | $6.7 \pm 0.7 \times 10^{-5}$ |
| $F_{0.2-8 \text{ keV}}^{\text{b}}$ ($\text{ergs cm}^{-2} \text{ s}^{-1}$)..... | 1.05×10^{-11} | 2.2×10^{-12} | 2.3×10^{-12} |
| L_{PL}^{c} (ergs s^{-1})..... | 1.8×10^{30} | 8.1×10^{30} | 1.2×10^{30} |
| $L_{\text{CBB}}^{\text{d}}$ (ergs s^{-1})..... | 5.8×10^{32} | 4.4×10^{32} | 3.2×10^{31} |
| $L_{\text{HBB}}^{\text{e}}$ (ergs s^{-1})..... | 5.7×10^{31} | 1.6×10^{31} | 1.6×10^{29} |
| Norm _{pn} ^f | Ti:1 (fixed); SW:1.05 | 1 (fixed) | ... |
| Norm _{MOS1} ^f | 0.96 | 0.98 | ... |
| Norm _{MOS2} ^f | ... | 1.07 | ... |
| χ^2/dof | 1.11 | 1.02 | 1.19 |
| dof..... | 368 | 327 | 73 |

NOTE.—To compute luminosities we assumed a distance of 288 pc for PSR B0656+14 (Briskin et al. 2003), of 750 pc for PSR B1055–52 (Kramer et al. 2003), and of 157 pc for Geminga (Caraveo et al. 1996).

^a Results from Caraveo et al. (2004).

^b Observed flux, 0.2–8 keV.

^c 0.5–10 keV luminosity of power-law component.

^d Bolometric luminosity of the cool blackbody component.

^e Bolometric luminosity of the hot blackbody component.

^f Normalization factor to account for calibration differences; Ti: fast-timing mode; SW: small-window mode.

computed at a 90% confidence level for a single interesting parameter. The lower temperature blackbody (hereafter “cool blackbody”) is associated with an emitting region with an area compatible with the full surface of the neutron star. The higher temperature component (“hot blackbody”) is seen to originate from a much smaller area. To visualize the correlation between different spectral parameters, we computed confidence con-

tours (at the 68%, 90%, and 99% levels for two parameters of interest) for the interstellar column density N_{H} versus the cool blackbody emitting area; this is shown in the insets in Figures 1, 2, and 3.

As shown in Figure 4, the overall shape of the spectrum of the Three Musketeers is very similar. However, remarkable differences in the luminosity of different spectral components

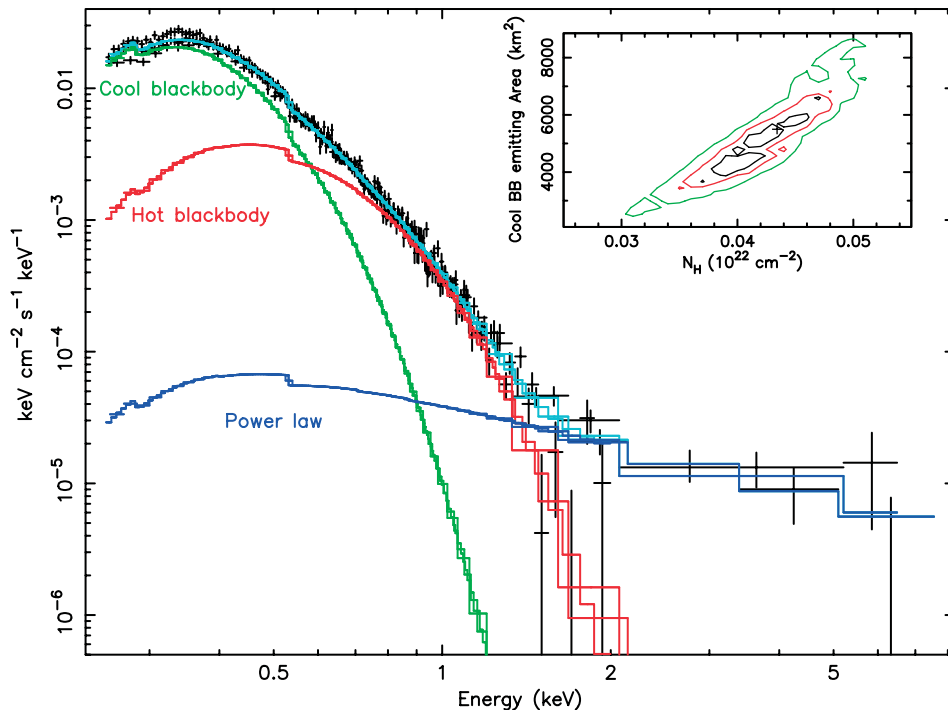


FIG. 2.—Same as Fig. 1, but for PSR B0656+14. Data from pn (both small-window and fast-timing mode) and MOS1 are plotted (*black points*). Detailed values of the best-fitting parameters are reported in Table 2.

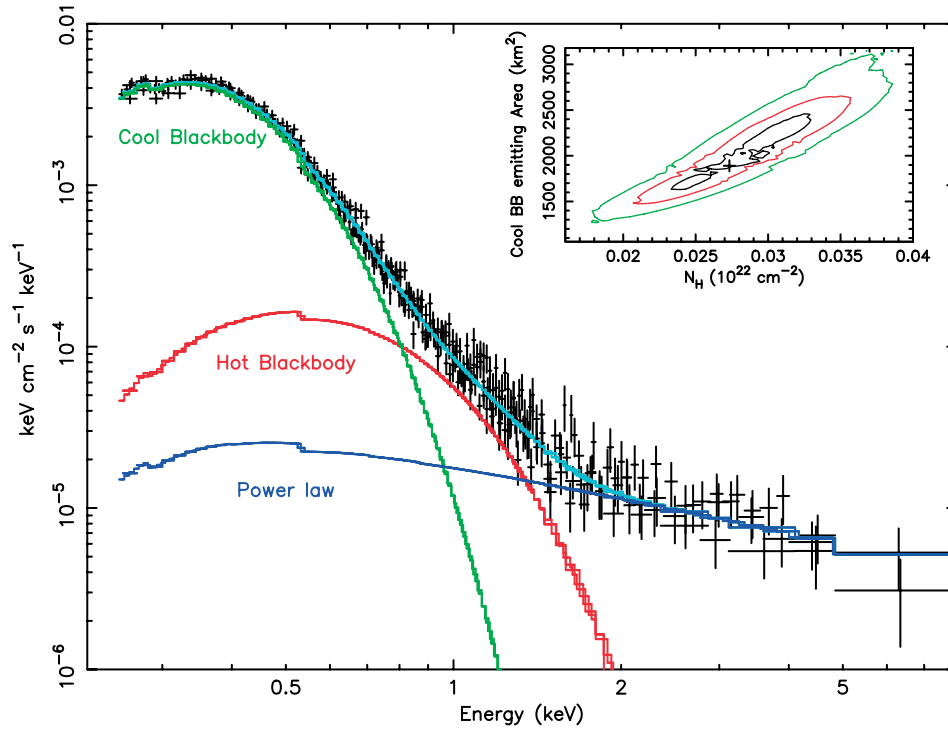


FIG. 3.—Same as Fig. 1, but for PSR B1055–52. Data are from pn, MOS1, and MOS2. See Table 2 for details on the best-fitting spectral parameters.

are immediately evident (see Table 2). In particular, we note that the luminosity of the hot blackbody in the case of Geminga is ~ 2 orders of magnitude lower than in the other two cases. At variance with PSR B0656+14 and PSR B1055–52, for Geminga the contribution of the power law dominates over the hot blackbody in the energy range where the hot blackbody has its maximum.

The parameters best fitting the EPIC spectrum of PSR B1055–52 (see Table 2) are fully consistent with the results reported by Becker & Aschenbach (2002) and by Pavlov et al. (2002), who included *ROSAT* data in their spectral fits to EPIC MOS and *Chandra* ACIS data, respectively. The same is true in the case of Geminga: although we use a three-component model, the results for the cool blackbody component (temperature

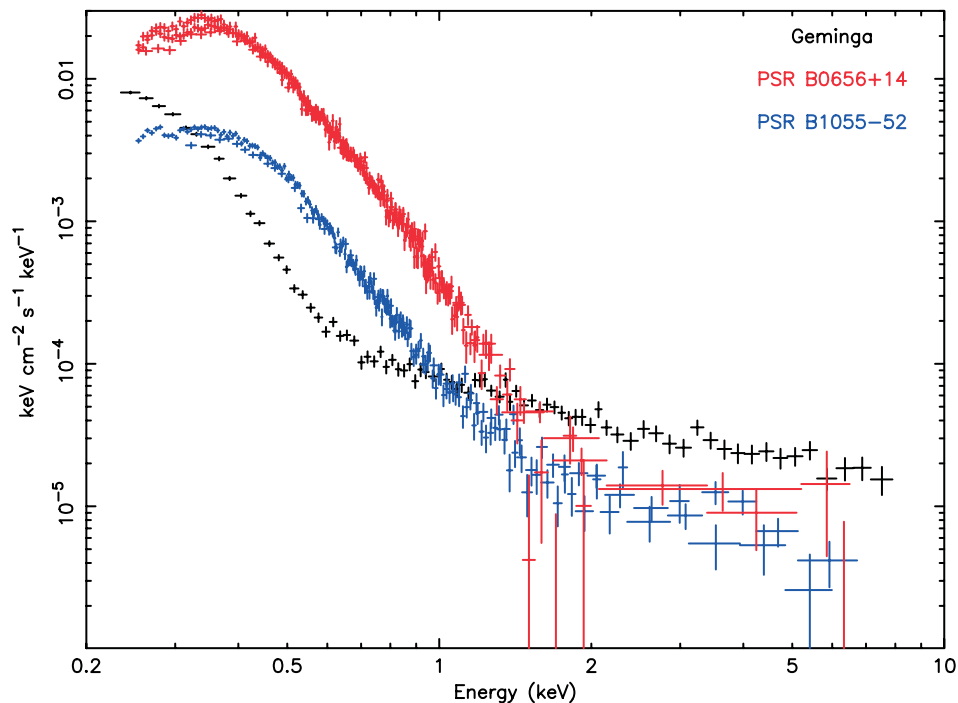


FIG. 4.—Unfolded spectra of PSR B0656+14 (red: data from pn and MOS1), PSR B1055–52 (green: data from pn, MOS1, and MOS2), and Geminga (black: data from pn). See text for details.

TABLE 3
RESULTS OF TIMING ANALYSIS

| Pulsar (1) | P Observed (ms) (2) | P Expected (ms) (3) |
|--------------------|-----------------------------|-----------------------------|
| PSR B0656+14 | 384.9029(2) | 384.90300043(5) |
| PSR B1055-52 | 197.111812(5) | 197.111809432(8) |
| Geminga | 237.1012(1) | 237.1012153(1) |

NOTES.—Col. (2): best period as computed from the EPIC X-ray data; col. (3): value expected on the basis of the extrapolation of published ephemeris. Sources: Kern et al. (2003) for PSR B0656+14, the ATNF data pulsar archive (<http://www.atnf.csiro.au/research/pulsar/psr/archive/>) for PSR B1055-52, and Jackson et al. (2002) for Geminga. The uncertainty quoted between parentheses refers to the least significant digit.

and emitting radius) are found to be very similar to those for *ROSAT* (see, e.g., Halpern & Ruderman 1993). The case of PSR B0656+14 is slightly different: the interstellar column density ($4.3 \pm 0.2 \times 10^{20} \text{ cm}^{-2}$) resulting from the simultaneous fit to the pn/fast-timing, pn/small-window and MOS1/full-frame data is larger than the values ($\sim 2 \times 10^{20} \text{ cm}^{-2}$) obtained by Pavlov et al. (2002) and Marshall & Schulz (2002) (based on *Chandra* ACIS/LETG data) and by Possenti et al. (1996) (based on *ROSAT* data). Thus, our analysis of the EPIC data results in a brighter underlying continuum at low energies, leading to a lower temperature coupled to a larger emitting surface for PSR B0656+14. Addressing such a discrepancy, possibly due to subtle cross-calibration issues, is beyond the scope of our fitting exercise, which was performed to provide the starting point for the phase-resolved spectroscopy of the EPIC data.

3.2. Timing Analysis

As a first step, we studied the high time resolution pn data in order to derive the period of our targets. Source photons were selected from the regions described above, in the energy range 0.15–8 keV for pn small-window mode and 0.15–2 keV for pn fast-timing mode.⁴ Photon arrival times were converted to the solar system barycenter using the SAS task *barycen* and folded using 10 bins in a range of trial periods around the expected values. A very significant detection of the pulsation was obtained in each case. To determine with higher accuracy the period value and to evaluate the corresponding error, we followed the prescription of Leahy (1987).

The results are reported in Table 3, in which they are compared with the extrapolations of the radio ephemeris, selected to be the ones nearest to the *XMM-Newton* observation. The period for the radio-quiet Geminga is compared with the γ -ray ephemeris of Jackson et al. (2002), on the basis of the analysis of the complete EGRET data set. A perfect consistency between the expected and measured values is apparent.

To align in phase the X-ray light curves with the radio (or γ) curves, we folded *XMM-Newton* data using the radio timing solutions for PSR B0656+14 and PSR B1055-52 and the γ solution for Geminga. The absolute accuracy of the *XMM-Newton* clock is $\sim 500 \mu\text{s}$, as stated by the calibration team (Kirsch 2004) and confirmed by recent investigations (e.g., Becker et al. 2004). The extrapolation of the radio ephemeris to the time of the *XMM-Newton* observations yields a phase uncertainty of ~ 0.01 for PSR B0656+14 (corresponding to one-

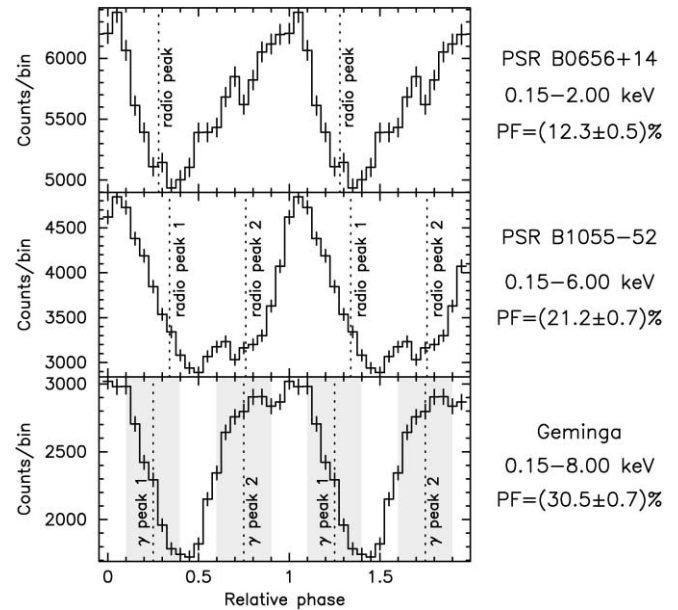


FIG. 5.—Light curves of the Three Musketeers. Data from pn (energy ranges: 0.15–2 keV for PSR B0656+14; 0.15–6 keV for PSR B1055-52; 0.15–8 keV for Geminga) have been folded using the radio timing solutions reported in Table 3 for PSR B0656+14 and PSR B1055-52 and the EGRET γ -ray ephemeris (also reported in Table 3) for Geminga. The phase has been set in order to put the X-ray maximum at phase 0. The phases of the radio peaks have been marked with vertical dashed lines; their uncertainty is estimated to be ~ 0.01 (1/5 of phase bin) for the case of PSR B0656+14 and ~ 0.003 ($\sim 1/20$ of phase bin) for PSR B1055-52. See text for further details. For PSR B1055-52 “radio peak 1” refers to the highest peak in the radio profile (see also Fig. 7). We also plotted the phases of the γ -ray peaks for Geminga; however, as discussed by Caraveo et al. (2004), the propagation of errors in the extrapolation of the EGRET ephemeris makes their position uncertain by ± 0.15 (such a phase interval corresponds to the gray-shaded regions; “ γ peak 1” refers to the highest peak in the γ -ray profile; see also Fig. 8).

fifth of a phase bin in Fig. 5) and of ~ 0.003 (1/20 of a phase bin in Fig. 5) for PSR B1055-52, for which the clock accuracy is the dominant factor, since the radio and X-ray data are almost simultaneous.

A larger uncertainty, ~ 0.15 in phase, is present in the case of Geminga, as discussed by Caraveo et al. (2004), because of the much longer time separation between the EGRET and *XMM-Newton* observations.

The folded pulse profiles (background subtracted) of our targets using the overall EPIC energy range are shown in Figure 5. To facilitate comparison, all the light curves have been plotted setting phase 0 to the X-ray pulse maximum as seen in the overall energy band. The phases of the radio peaks (PSR B0656+14 and PSR B1055-52) and γ -ray peaks (Geminga and PSR B1055-52) are also shown. Pulsed fractions have been computed as the ratio between the counts in excess of the minimum and the total number of counts, deriving the corresponding uncertainties from the propagation of the statistical errors in the folded light curves.

Next we studied the variations of the pulse profiles with energy. The light curves relative to four energy intervals are shown in Figure 6 (PSR B0656+14), Figure 7 (PSR B1055-52), and Figure 8 (Geminga). Note that the energy ranges used are different for different targets, since for each source the energy intervals have been chosen to visualize the light curve relative to the cool blackbody, transition region, hot blackbody, and power law. The bottom panels of Figures 6 and 7 show the radio profile of PSR B0656+14 and PSR B1055-52 at

⁴ Time-tagging of photons is reliable over the whole detector sensitivity range; therefore, we also include low energy ($E < 0.25 \text{ keV}$) photons in the timing analysis, which are not used for spectroscopy (see § 3.1)

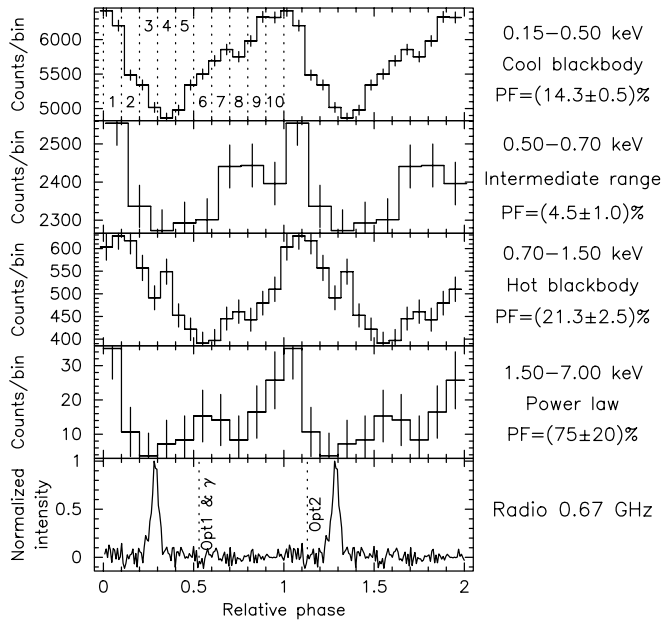


FIG. 6.—Light curves of PSR B0656+14 in different energy ranges. Data (obtained with pn fast-timing mode observations, with the exception of the hardest band, which is based on pn small-window mode data) have been folded using the radio ephemeris quoted in Table 3. The alignment in phase is the same as that chosen for Fig. 5. Although always single peaked, the pulse profile changes significantly going from the softest energy range (dominated by the cool blackbody) to the 0.7–1.5 keV range (dominated by the hot blackbody). Note the minimum in the pulsed fraction in the intermediate 0.5–0.7 keV range. Above 1.5 keV the lack of statistics hampers a detailed study of the pulse profile. The radio light curve is shown in the bottom panel. The uncertainty on the phase alignment of the X-ray light curve with the radio curve is ~ 0.01 . The single radio pulse is seen to trail the X-ray maximum by ~ 0.2 in phase. The phases of the two optical peaks (Kern et al. 2003), as well as of the γ -ray peak claimed by Ramanamurthy et al. (1996), are also shown. See text for further details.

0.67 GHz.⁵ For the case of Geminga (Fig. 8), the γ -ray light curve⁶ is shown. Ten phase intervals, selected a priori to be used for phase-resolved spectroscopy (see § 3.3), are marked in the top panels. Our three neutron stars exhibit vastly different phenomenologies. The main results may be summarized as follows (see also the legends of Figs. 6, 7, and 8).

1. For PSR B0656+14 a single pulse per period may be seen in each energy band. The pulse shape below 1.5 keV is broadly sinusoidal; a significant change in pulse profile occurs between the energy range dominated by the cool blackbody and the range dominated by the hot blackbody. As a consequence, in the intermediate range the pulsed fraction reaches its minimum value. At higher energy, the pulse profile seems sharper, although the few statistics do not allow us to study its shape (or the pulsed fraction) with great accuracy. Note that the light curve above 1.5 keV was obtained by folding data from the short pn small-window mode observation; the other cases represent data from the longer fast-timing observation. Considering the overall light curve (Fig. 5), the single radio peak lags behind the X-ray maximum by $\sim 0.25 \pm 0.05$ in phase (the uncertainty is dominated by the X-ray light-curve bin width for

⁵ Retrieved from the European Pulsar Network database, at <http://www.mpifr-bonn.mpg.de/div/pulsar/data/browser.html>.

⁶ This was obtained by selecting nine EGRET viewing periods in which the target was imaged close to the center of the field of view and had good photon statistics; events with energy $E > 100$ MeV were extracted from the source position; arrival times were converted to the solar system barycenter and folded with the ephemeris published by Jackson et al. (2002).

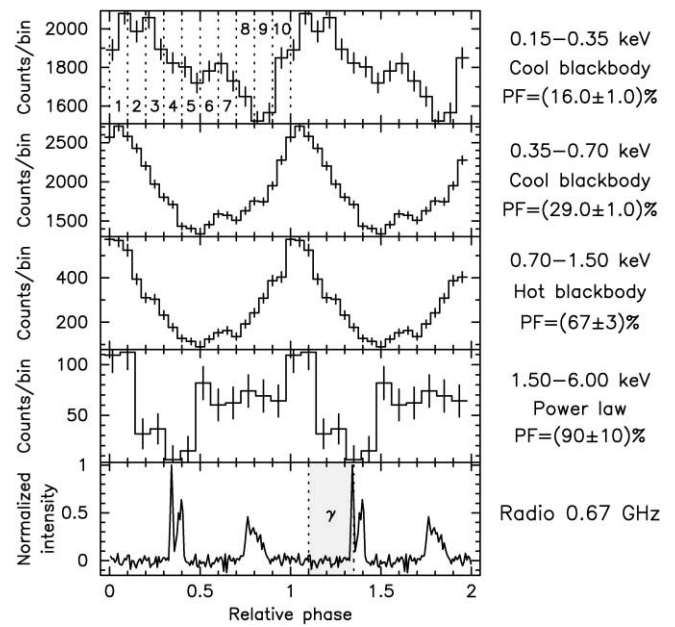


FIG. 7.—Light curves of PSR B1055-52. Note the broader profile of the X-ray pulse below 0.35 keV and the small (~ 0.1) phase shift with respect to higher energies. Note the value of the pulsed fraction, which grows with energy and is remarkably high ($\sim 70\%$) in the 0.7–1.5 keV range, where the neutron star emission is dominated by the hot blackbody component. For a more detailed study of the energy resolved pulsed fractions see Becker & Aschenbach (2002). Above 1.5 keV the low S/N hampers a detailed study of the pulse profile. We plotted the radio light curve in the bottom panel. The uncertainty on the phase alignment is of ~ 0.003 . The two radio peaks are observed to bracket the single X-ray peak. The γ -ray pulse (Thompson et al. 1999) occurs in the gray-shaded phase interval between the two vertical dashed lines.

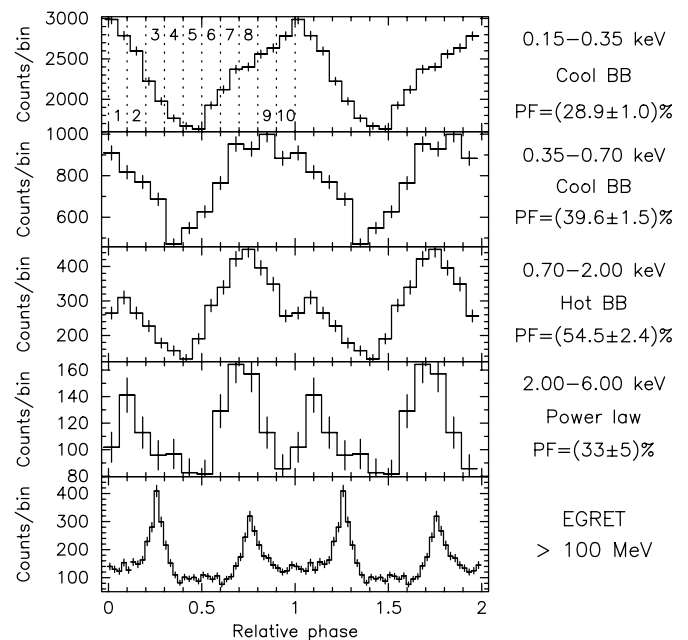


FIG. 8.—Light curves of Geminga. As discussed by Caraveo et al. (2004), the pulse shape changes as a function of energy. The single, broad peak observed at low energy (at which emission from the cool blackbody dominates) changes to two peaks at higher energies (where the power-law component dominates). The pulsed fraction is maximum in the 0.7–2 keV range, in which the hot blackbody component is more important. The bottom panels show the EGRET γ -ray light curve. The extrapolation of the γ -ray ephemeris makes the absolute phase alignment uncertain by ± 0.15 , owing to the long time span between the EGRET and the EPIC observations. Note that the numbering of the phase intervals defined in the top panel is different from that used by Caraveo et al. (2004). Their phase 1 is phase 3 here, and similarly for the others.

the determination of the position of the X-ray peak), occurring very close to the X-ray minimum. In the bottom panel of Figure 6 we mark the phases of the double-peaked pulse profile observed in the V band by Kern et al. (2003). The position of the single γ -ray peak claimed by Ramanamurthy et al. (1996) is also indicated.

2. PSR B1055–52 also shows a single pulse per period at all energies, with a markedly different shape in the softest band (less than 0.35 keV) with respect to intermediate energy ranges (0.35–1.5 keV), while in excess of 1.5 keV the low S/N hampers study of the pulse profile. The pulsed fraction, which is seen to grow with energy, is remarkably high ($\sim 70\%$) in the band in which the hot blackbody dominates the neutron star emission. The two peaks of the radio profile are seen to follow the contour of the X-ray peak at all energies; in the overall light curve the highest radio peak lags behind the X-ray peak by $\sim 0.2 \pm 0.05$ (the uncertainty is dominated by the X-ray light-curve binning). The phase interval in which the γ -ray pulse occurs lies between the X-ray maximum and the highest radio peak.

3. Geminga shows a different behavior of the pulse shape as a function of energy. The single, broad peak seen at low energy, at which the cool blackbody dominates, changes to a double peak toward higher energies, at which the bulk of the emission is non-thermal (power-law component). The pulsed fraction reaches a maximum of $>50\%$ in the energy range in which the hot blackbody is more important. The significant uncertainty (~ 0.15) affecting the extrapolation of the EGRET ephemeris (see above) prevents any firm conclusion on the alignment between the X-ray and γ -ray light curves.

3.3. Phase-resolved Spectroscopy

The results of the spectral and timing analysis were then used to study the variation of the emission spectrum with pulse phase. For both PSR B0656+14 and PSR B1055–52 we selected photons whose arrival times fall into the 10 different phase intervals marked on Figures 6 and 7. The time resolution of both the pn fast-timing mode (0.03 ms) and small-window mode (5.6 ms) is adequate to perform such photon phase selection. We then extracted 10 phase-resolved spectra. For the case of PSR B0656+14 this was independently done for both fast-timing and small-window data. Each spectrum was then rebinned in order to have at least 40 counts per bin. Since now we are interested to study *relative* variations as a function of the pulsar phase, we did not add systematic errors to the pn phase-resolved spectra.

As already suggested by the analysis of the energy-resolved pulse profiles, the spectra of both sources do vary as a function of the pulsars' rotational phase. This is easily seen in the first column of Figures 9a and 9b (PSR B0656+14) and Figures 10a and 10b (PSR B1055–52), in which the observed phase-resolved spectra are compared with the best-fit model describing the phase-averaged ones and the deviations are computed in units of statistical standard errors.⁷ The variation is dramatic in the case of PSR B1055–52, because of the high phase modulation of its emission (up to 70% in the 0.7–1.5 keV range; see Fig. 7), while it is less spectacular (but still seen with high significance) for PSR B0656+14, because of its lower modulation (pulsed fraction $\leq 20\%$ below 2 keV; see Fig. 6). Note that in the case of PSR B0656+14 phase-resolved spectra have

been rebinned in order to ease the visibility of the modulation on the graphs' scale. PSR B0656+14 and PSR B1055–52 seem therefore to share the same characteristics seen in Geminga, but their behaviors follow different trends (the case of Geminga is reported in Figs. 11a and 11b).

Turning now to the spectral fit of the phase-resolved spectra, no meaningful results could be obtained by allowing both the temperature and the normalization of the blackbodies to vary: a definite trend showing the maximum temperature in correspondence to minimum emitting area (and vice versa) was systematically obtained in all cases. Such a modulation pattern is obviously driven by the strong correlation between the two spectral parameters and cannot be trusted as reliable.

Thus, we used the phase-integrated best-fit model as a template to describe the phase-resolved data. The N_{H} value, the temperatures of both blackbodies and the power-law photon index were fixed to the values best fitting the phase-integrated spectrum. The phase modulation was then reproduced by allowing the normalization parameters of each spectral component to vary independently. For the case of PSR B0656+14, spectra from small-window data and from fast-timing data corresponding to the same phase interval were fitted simultaneously.

As in the case of Geminga (Caraveo et al. 2004), such a simple approach (using only three free parameters) yielded a satisfactory description of the phase-resolved spectra also for PSR B0656+14 and PSR B1055–52. Reduced χ^2 -values of ~ 0.8 –1.4 were obtained in different phase intervals.

The results of phase-resolved spectral fits are shown in the right column of Figs. 9a and 9b, 10a and 10b (the case of Geminga is represented in Figs. 11a and 11b): for each phase interval, the three best-fitting spectral components are plotted, superposed on the unfolded data points.

Knowing the objects' distance values, we can then compute the emitting surface corresponding to each blackbody curve. To visualize the evolution of the spectral parameters as a function of the pulsars' phase, we plotted the blackbody radii, as well as the power-law intensities, as a function of the objects' rotational phase. This is shown in Figures 12, 13, and 14.

The behavior of the three neutron stars as a function of their rotational phase is vastly different. The most important results may be summarized as follows.

1. The cool blackbody component shows a similar phase evolution for the three targets. The values of the blackbody radii follow a roughly sinusoidal profile with a modulation $\leq 10\%$ (with respect to the average value) for PSR B0656+14 and PSR B1055–52 and of $\sim 15\%$ for Geminga.

2. The hot blackbody components have a similar phase evolution with a sinusoidal profile. However, we see striking differences both in the amplitude of their phase modulation and in their overall luminosity. While for PSR B0656+14 the modulation in the emitting radius with respect to the average value is $< 10\%$, similar to the value found for the cool blackbody component, in the case of PSR B1055–52 we see a 100% modulation, since the hot blackbody component is not seen in four out of 10 phase intervals. A similar, 100% modulation is also observed in the case of Geminga, although in this case the hot blackbody component is seen to disappear in just one phase interval, and the profile of its phase evolution is markedly broader. As far as the radii values are concerned, we note that they span a factor of 30, ranging from the 60 m of Geminga to the ~ 2 km of PSR B0656+14.

3. The study of the power-law component is partially hampered, in the cases of PSR B0656+14 and PSR B1055–52, by

⁷ An animated version of Figs. 9a and 9b, 10a and 10b, and 11a and 11b is available at <http://www.mi.iasf.cnr.it/~deluca/3musk/>.

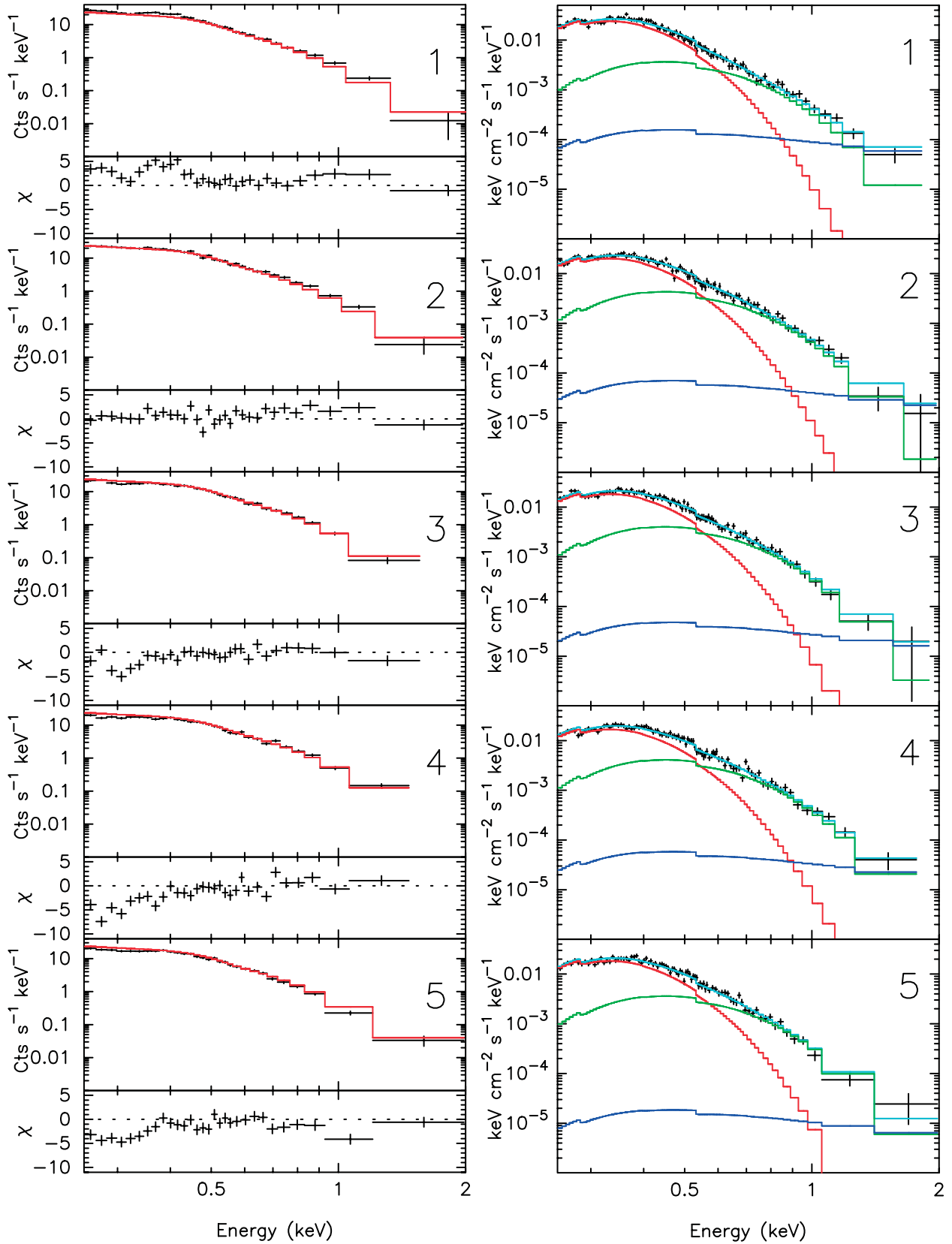


FIG. 9a

FIG. 9—(a) Phase-resolved spectra of PSR B0656+14. Photons have been selected in correspondence to the phase intervals marked in Fig. 6. Phase intervals from 1 to 5 are shown here; phase intervals 6–10 are shown in Fig. 9b. The top panels on the left present, for each phase interval, the observed spectrum (*data points*) compared with the best-fit model (*solid line*) of the phase-integrated spectrum (*upper plots*); the lower panels show the difference between data and such model in units of statistical errors. To ease the visibility of the deviations of phase-resolved spectra from the averaged spectrum template, spectral channels have been rebinned. The panels on the right show, for each phase interval, the unfolded spectrum together with its best-fit model. The model components are also plotted (colors as in Fig. 2). Animated versions of Figs. 9a, 9b, 10a, 10b, and 11a, 11b are available at <http://www.mi.iasf.cnr.it/~deluca/3musk/>. (b) Same as (a), but for phase intervals 6–10.

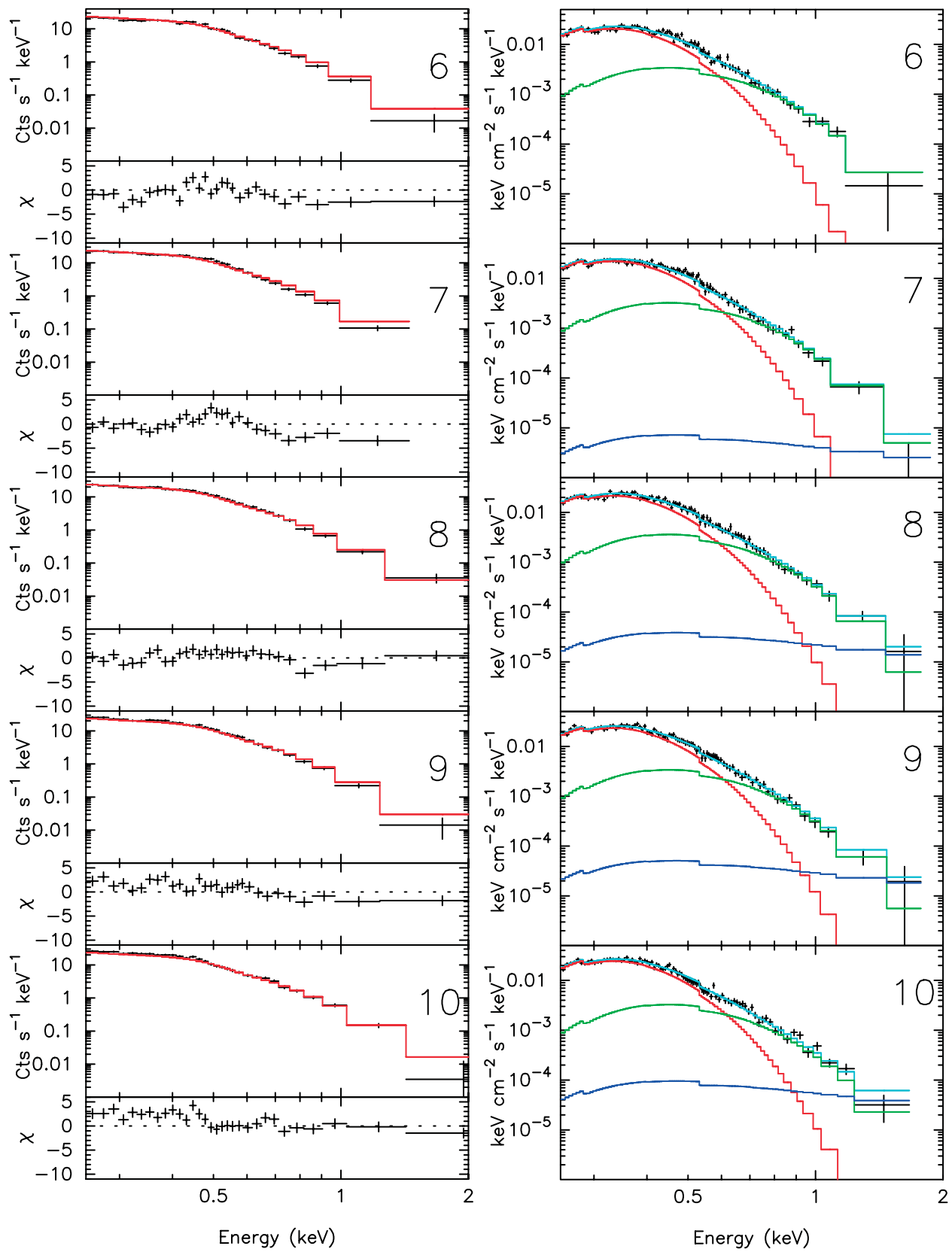


FIG. 9b

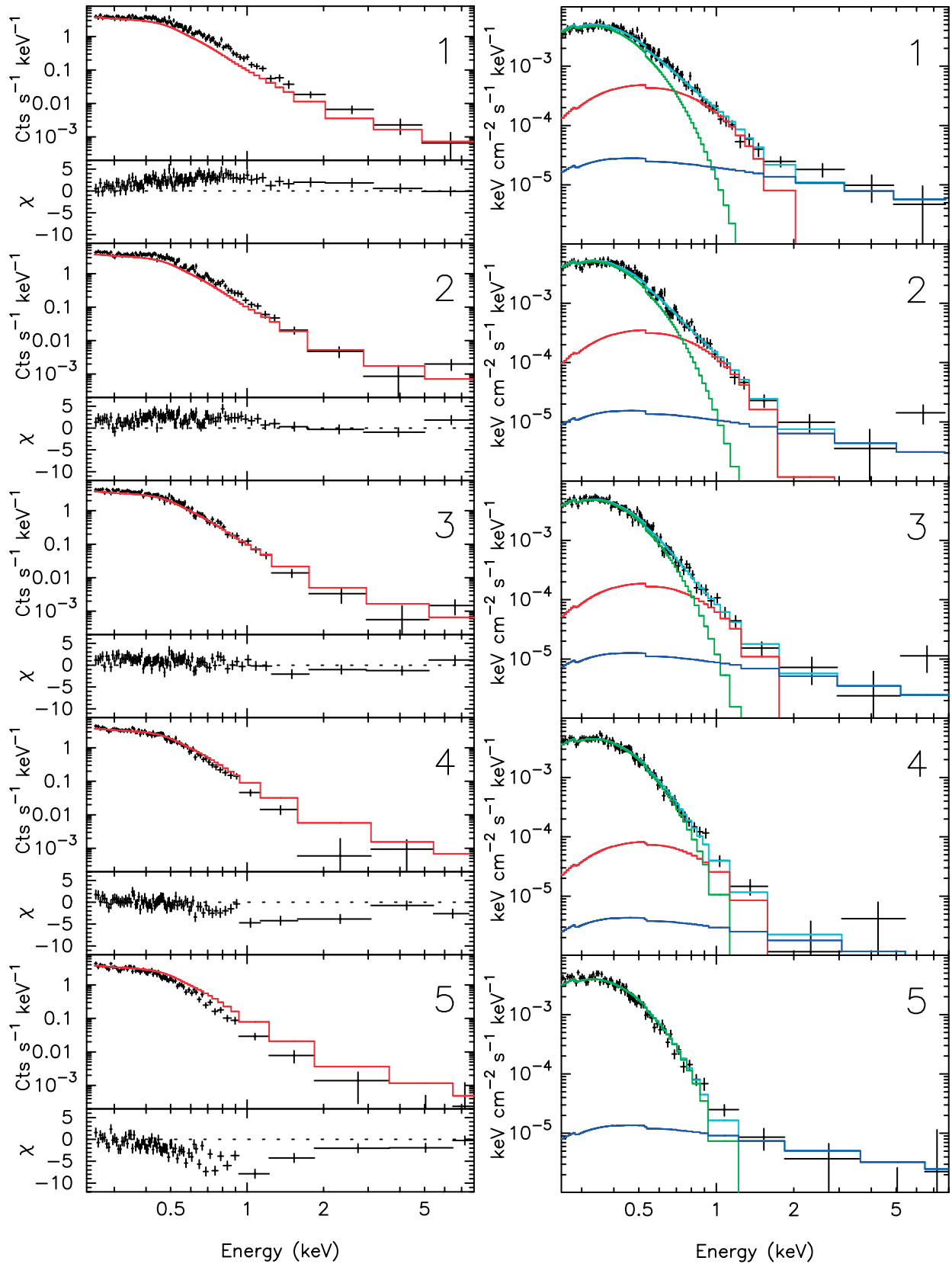


FIG. 10a

FIG. 10.—(a) Phase-resolved spectra of PSR B1055–52. Phase intervals 1–5 (according to the notation of Fig. 7). See the Fig. 9a legend for explanations. Data have not been rebinned. Note the much higher deviations of the phase-resolved spectra with respect to the average one. (b) Same as (a), but for phase intervals 6–10.

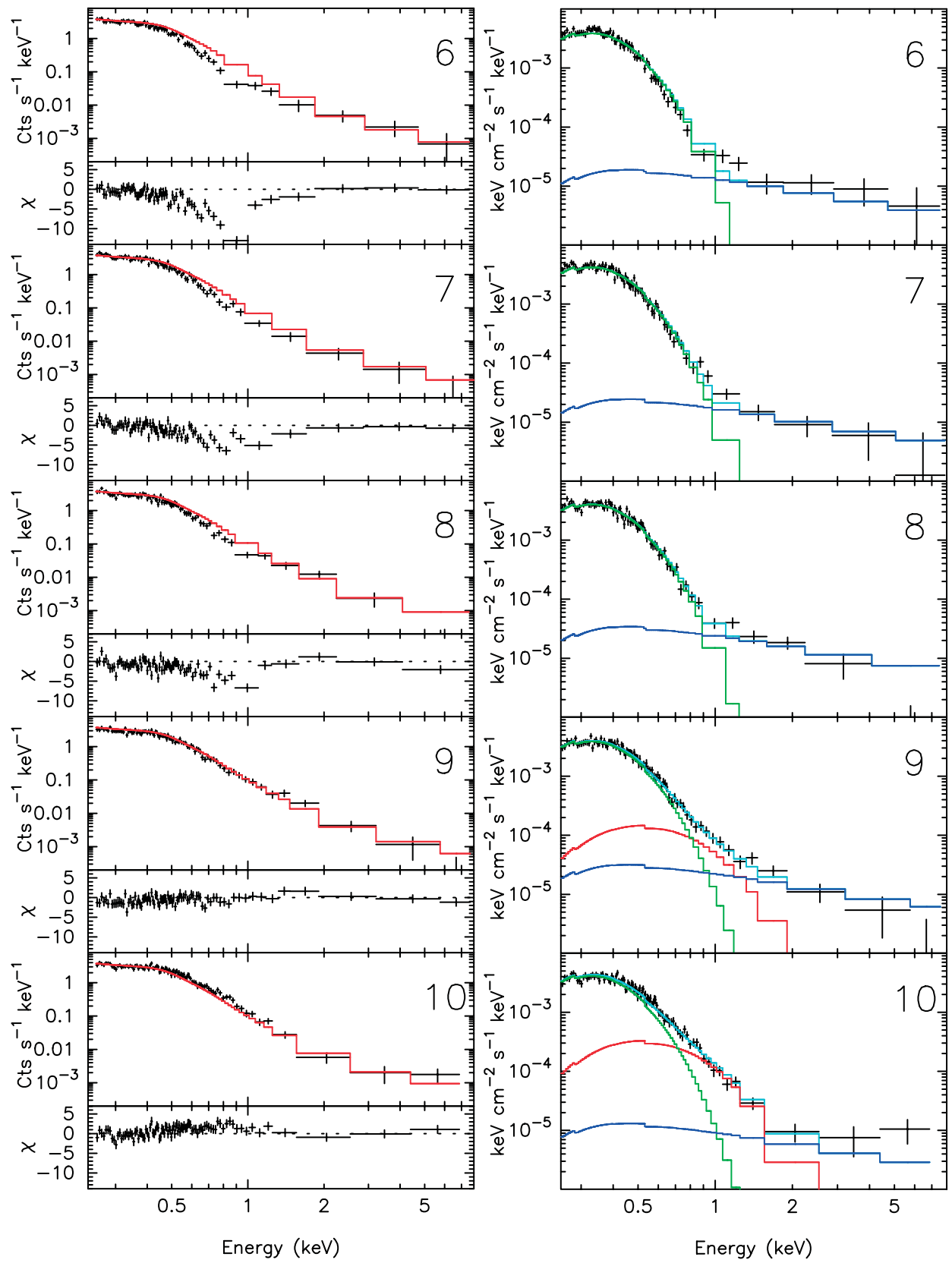


FIG. 10b

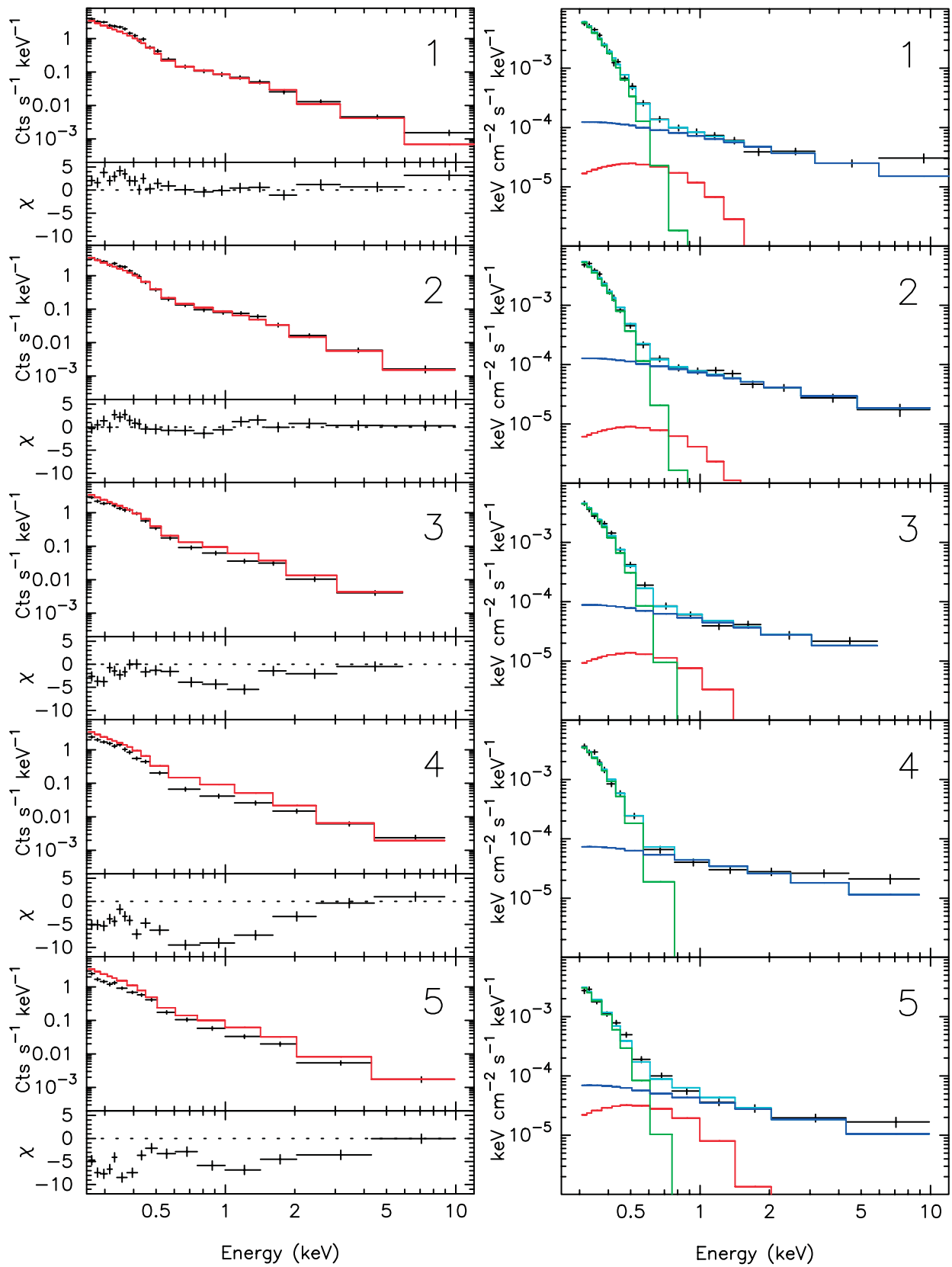


FIG. 11a

FIG. 11.—(a) Phase-resolved spectra of Geminga. Phase intervals 1–5 (see Fig. 8). See the Fig. 9a legend for explanations. The figure is adapted from Caraveo et al. (2004) but presented according to the phase numbering and color code adopted in this work. (b) Same as (a), but for phase intervals 6–10.

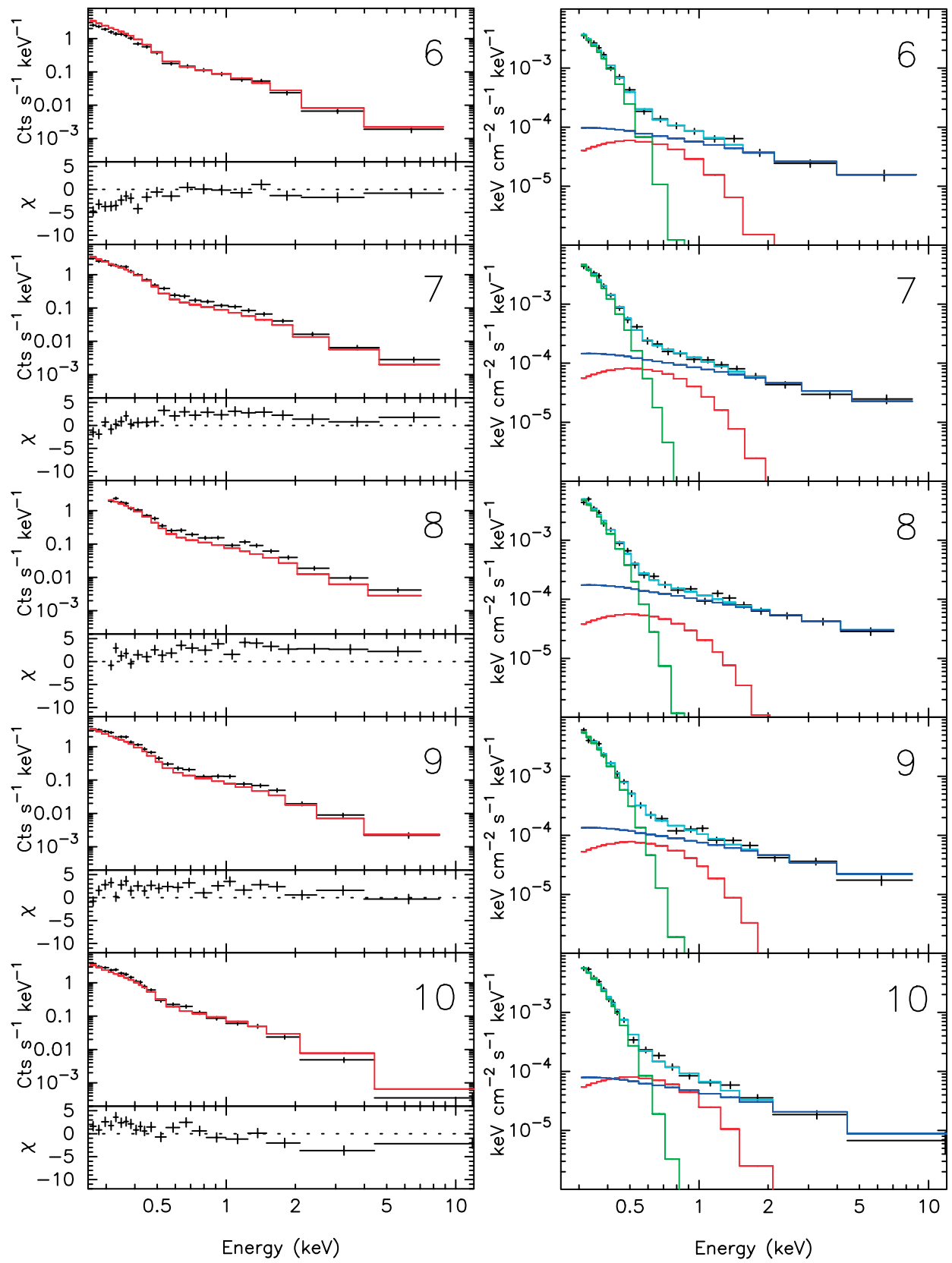


FIG. 11b

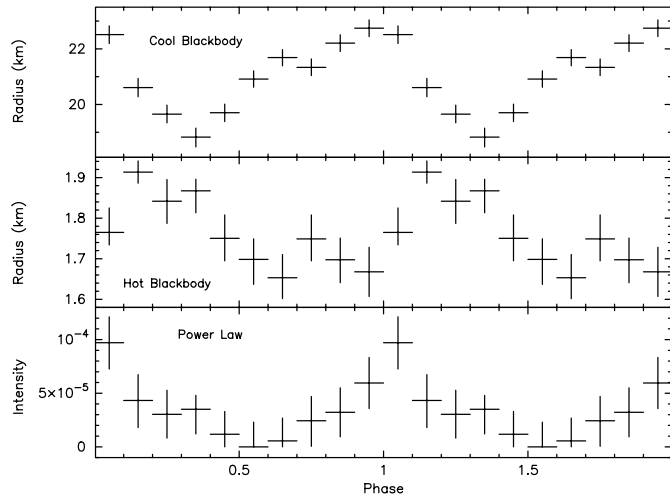


FIG. 12.—Parameters best fitting the phase-resolved spectra of PSR B0656+14 plotted as a function of the pulsar phase, defined as in Fig. 5. Both cool and hot blackbody emitting surfaces evolve throughout the pulsar phase following a sinusoidal pattern showing an overall $\sim 10\%$ modulation (with respect to the average values) on the emitting radii value. Note the marked anticorrelation between the top two panels with the hot blackbody peaking in correspondence of the cool blackbody minimum. The power-law component has a different phase trend with respect to the thermal components, with a single, sharper peak.

the low S/N at energies in excess of 1.5 keV because of the high background affecting the fast-timing observations. It is therefore difficult to assess the shape of the pulse profile (single peaked for PSR B0656+14? double peaked for PSR B1055–52?) and the actual modulation in such cases. Conversely, for Geminga, thanks to the different pn mode, the power-law component shows a clear double-peaked profile, with a significant unpulsed flux.

4. The relative phase evolution of the three spectral components is vastly different for the three neutron stars. This is particularly evident when looking at the two blackbody com-

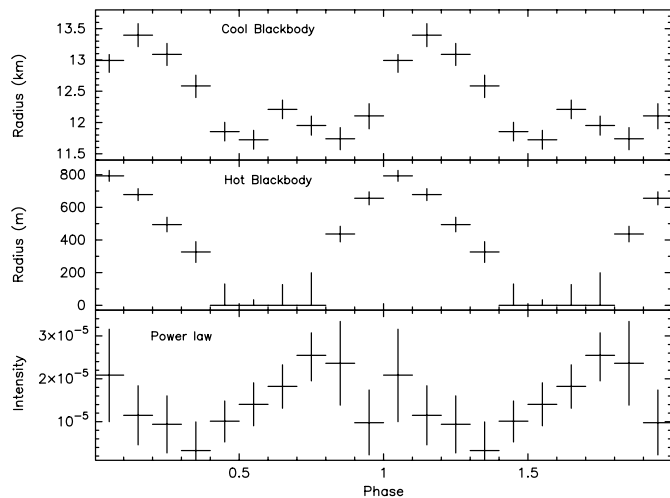


FIG. 13.—Same as Fig. 12, but for PSR B1055–52. While the cool blackbody emitting radius shows a $<10\%$ modulation (with respect to the average value), the hot blackbody component shows a dramatic, 100% modulation since its contribution is null in four of the 10 phase intervals. Note that for PSR B1055–52 the two thermal components have a similar time evolution, with a phase shift as low as ~ 0.1 . The power-law component has a different modulation; it is difficult to assess whether its profile is single peaked or double peaked, because of the lower S/N in the high-energy portion of the spectra.

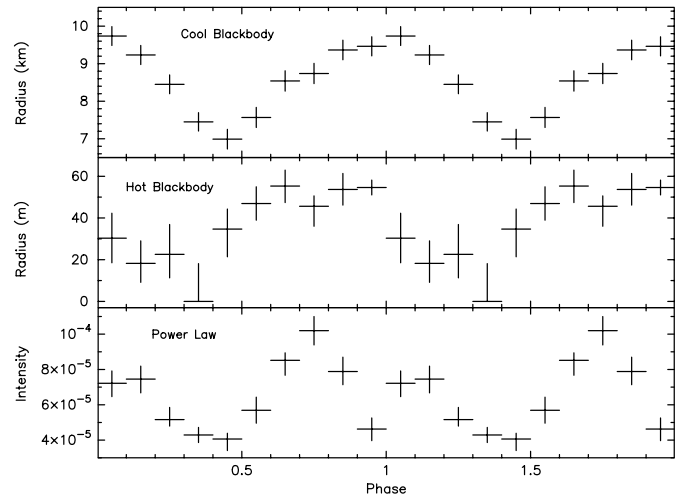


FIG. 14.—Same as Figs. 12 and 13, but for Geminga. The figure is adapted from Caraveo et al. (2004; see their Fig. 4) according to the choice of phase adopted in this work. The cool blackbody component shows a $\sim 15\%$ modulation (with respect to the average value) of its emitting radius, with a sinusoidal profile. Conversely, the hot blackbody is 100% modulated and disappears for 1/10 of the pulsar period. The power-law component has a remarkably different, double-peaked phase profile and shows a significant unpulsed fraction.

ponents. In the case of PSR B0656+14 some sort of anticorrelation is observed, with the hot blackbody peaking in correspondence to the cool blackbody minimum. This is at odds with the behavior observed for PSR B1055–52, in which the two thermal components appear definitely correlated. Geminga shows an intermediate phenomenology: the cool and the hot blackbodies have a ~ 0.25 difference in their phase pattern.

Of course, one could fit the phase-resolved spectra, fixing the emitting radii to the average values and leaving the temperatures as free parameters. The goodness of the fits obtained following such an approach is comparable to that obtained previously by fixing the temperatures and the photon index. Not surprisingly, the evolution of the parameters, as a function of the phase, is very similar to the plots shown in Figures 12, 13, and 14. However, such an approach renders less immediate the interpretation of the hot blackbody phase evolution, especially in the case of PSR B1055–52, in which the hot spot is not present for about half of the period. Maximum emitting radius translates into maximum temperature; absence of hot spot translates into $T(\text{hot blackbody}) = T(\text{cool blackbody})$, implying important changes of temperature for the same polar cap, indeed a small portion of the neutron star surface.

4. DISCUSSION

The phase-resolved spectroscopy of PSR B0656+14, PSR B1055–52, and Geminga allows for a new view of the phenomenology of these middle-aged neutron stars. While the phase-averaged spectra of our targets look very similar, their phase-resolved behavior is quite different. This is particularly evident from Figures 12, 13, 14, in which the evolution of the cool and hot blackbody-emitting radii, as well as of the power-law flux, is shown as a function of the pulsars' phase. Because of the less than optimal quality of data collected for PSR B0656+14 and PSR B1055–52 above 2 keV, here we concentrate on the analysis of the two thermal components, which presumably come from the star surface, albeit from different regions at different temperatures.

4.1. The Cooler Component

First, let us examine the cooler component. It is seen to come from a region encompassing a good fraction, if not the totality, of the neutron star surface as a result of the star cooling. We note that the best-fitting emitting surface in the case of PSR B0656+14 is very large (observed emitting radius of ~ 21 km) if compared with expectations for a standard neutron star. Distance uncertainties cannot ease the problem, because of the very accurate radio VLBI parallax measurement (Briskin et al. 2003). In any case, a value of 15 km, corresponding to a somewhat stiff equation of state (see Lattimer & Prakash 2001 and references therein), is marginally compatible with the data (being allowed within the 99% confidence contour plot for N_H and the emitting surface shown in Fig. 2). The pulsed fraction observed in the energy range in which the cooler component dominates is 14% for PSR B0656+14 (Fig. 6) and 16% for PSR B1055–52 (Fig. 7), while for Geminga it is greater than 30% (Fig. 8).

We ascribe this modulation to a variation of the emitting areas, ranging from a sizeable fraction to the totality of the neutron star surface as a function of the rotational phase. A viable mechanism to provide some sort of phase-dependent “obscuration” of the bulk of the neutron star surface could be the magnetospheric “blanket,” originally described by Halpern & Ruderman (1993) in their study of the soft thermal emission from Geminga (see also Halpern & Wang 1997). Cyclotron resonance scattering by plasma in the magnetosphere at a few stellar radii could screen the thermally emitting surface during specific phase intervals, depending on the magnetic field configuration and viewing geometry.

Alternatively, the flux variations could also be due to large-scale surface temperature modulations, expected as a consequence of anisotropic heat transfer from the neutron star interior (Greenstein & Hartke 1983). As discussed in § 3.3, this interpretation is consistent with the observed spectral phase variation as well. With current data we are not able to disentangle temperature and emitting surface variation without a complete physical model. We note that the observed pulsed fraction values are much greater than expected on the basis of simple thermal models. As shown by Page (1995), modulation of a few percent is expected in large-scale surface thermal emission, owing to the effects of gravitational bending. Pulsed fractions as high as the observed values could be explained by assuming a peculiar beaming of the thermal surface emission. Because of anisotropic radiative transfer in a magnetized plasma, an anisotropic angular emission pattern with respect to the surface’s normal one, is indeed expected, depending on temperature and magnetic field intensity and configuration⁸ (e.g., Zavlin & Pavlov 2002 and references therein).

4.2. The Hot Spot(s)

Turning now to the hotter component, we note that for all objects this is the most dramatically variable spectral component. It is natural to interpret such marked variations as an effect of star rotation, which brings into view and hides one or more hot spots on the star surface. It is commonly accepted that neutron stars should have polar caps hotter than the rest of the surface. This could be due to different processes, such as the bombardment of charged particles accelerated in the magnetosphere and falling back to the polar caps along magnetic field lines (return currents; see, e.g., Ruderman & Sutherland 1975;

Arons & Scharlemann 1979) or anisotropic heat transfer from the neutron star core, which depends strongly on the magnetic field direction and is maximum along the magnetic field lines (see, e.g., Greenstein & Hartke 1983). An association of the observed rotating hot spot(s) with the neutron stars’ polar caps seems therefore rather obvious.

4.2.1. Luminosity and Size

The observed hot spot bolometric luminosities vary by greater than 2 orders of magnitude from the rather similar values found for PSR B0656+14 and PSR B1055–52 (5.7×10^{31} and 1.6×10^{31} ergs s^{-1} , respectively), to the much dimmer Geminga (1.6×10^{29} ergs s^{-1}). The former two cases are in broad agreement with the theoretical expectations of Harding & Muslimov (2002) for polar cap heating due to downstreaming of $e^{+/-}$ generated by curvature radiation photons. In the case of the Geminga pulsar, close to the death line for creation of $e^{+/-}$ couples via curvature radiation, the lower polar cap luminosity is consistent with expectations for polar cap heating due to bombardment by particles created by inverse Compton scattered photons only (Harding & Muslimov 2002; see Caraveo et al. 2004).

Straight estimates of neutron star polar cap size, based on a simple “centered” dipole magnetic field geometry [polar cap radius $R_{PC} = R(R\Omega/c)^{1/2}$, where R is the neutron star radius, Ω is the angular frequency, and c is the speed of light), predict very similar radii for the three neutron stars, characterized by similar periods (233 m for PSR B0656+14, 326 m for PSR B1055–52, and 297 m for Geminga, assuming a standard neutron star radius of 10 km). The observed emitting radii are instead markedly different, with values ranging from ~ 50 m for Geminga to ~ 2 km for PSR B0656+14. Psaltis et al. (2000) showed that the observed polar cap radius may be different from the actual one by a large amount because of geometrical effects. Indeed, Caraveo et al. (2004) proposed a highly inclined viewing angle to reduce the surface of the emitting region in the case of Geminga. PSR B0656+14 and PSR B1055–52 face a completely different situation, since their polar caps are significantly larger than expected. Standard estimates, based on pure geometrical considerations, are clearly unsatisfactory. Even using the unrealistically large neutron star radius found for PSR B0656+14, the inferred polar cap dimension is < 600 m, far less than the hot spot radius. It is also possible, as suggested by Ruderman (2004), that thermal photons be significantly reprocessed higher up in the magnetosphere, interacting with charged particles. In such a picture, the same mechanism possibly providing the bulk of the cool blackbody modulation (via the phase-dependent screening quoted in § 4.1) would obviously bias all emitting radii (and temperatures) measurements based on blackbody fits.

4.2.2. Modulation with Phase

The observed phase modulation of the hot blackbody component is largely different for the three neutron stars in both amplitude and pattern. In the case of PSR B1055–52 a 100% modulation is seen, and the hot spot disappears for 4/10 of the pulsar period. This phenomenology strongly argues for an oblique rotator seen at high inclination. This would favor the historical Rankin (1993) interpretation of the radio polarization pattern of this pulsar (orthogonal rotator) versus the older one (almost aligned rotator) of Lyne & Manchester (1988); however, the presence of only one visible “pole” would represent a challenge for a classical orthogonal rotator seen at high inclination. Conversely, the much lower modulation observed in the case of PSR B0656+14 seems consistent with an almost

⁸ However, as noted in § 3.1, current atmospheric models do not yield a satisfactory description of the spectra of the Three Musketeers.

aligned rotator, with the polar cap always in sight. This picture is in good agreement with the radio pulse polarization results of Everett & Weisberg (2001), as well as with the above-mentioned studies of Rankin (1993) and Lyne & Manchester (1988). The remarkably high pulsed fraction of PSR B1055–52 ($\sim 70\%$ in the 0.7–1.5 keV range) requires a significant beaming of the hot thermal component emission. Indeed, Psaltis et al. (2000) estimated that under standard assumptions about the star mass and equation of state, a pulsed fraction higher than 35% cannot be produced even in the most “optimistic” case of an orthogonal rotator having very small polar caps with a high temperature contrast with respect to the rest of the star surface. The same consideration applies to the case of Geminga (pulsed fraction of $\sim 55\%$ in the 0.7–2 keV range but with a significant contribution of nonthermal emission). In all cases a single peak per period is observed. This may suggest that we are seeing a single hot region on the surface of the star. The visibility of a single pole along the star rotation is consistent with the geometrical interpretation of the phase-resolved behavior of PSR B0656+14, while for PSR B1055–5 an important role should be invoked for beaming to explain why the opposite pole emission is not seen in spite of the effects of gravitational light bending (Zavlin et al. 1995). An alternative possibility could be a magnetic field configuration different from a standard centered dipole. In the case of a magnetic field with significant multipole components, two (or more) hot polar caps could be very close on the star surface, and their emission could be blended in a single peak.

4.3. Phase Alignment between the Thermal Components

Because of the sensitivity of heat transfer to the magnetic field, a temperature anisotropy should exist on the neutron star surface, with temperature increasing toward the magnetic poles (e.g., Greenstein & Hartke 1983). Assuming the angular distribution of the radiation emitted by a surface element to be peaked along the normal to the surface and decrease toward larger angles (see Harding & Muslimov 1998 and references therein), we would expect the overall emission of the neutron star to be modulated as the poles come in and out of our line of sight. In particular, maximum flux should be observed when the line of sight is best aligned with the hotter regions. If the hot spots are indeed at the magnetic poles, a definite correlation between the hotter and colder components should be clearly visible in the phase evolution of the emitting regions. While this is indeed the case for PSR B1055–52, the contrary is true for PSR B0656+14, which shows a clear anticorrelation. Geminga shows an intermediate phenomenology, with a phase difference of ~ 0.25 between the hot and cool components (Fig. 14). Thus, at least one of the assumptions in the above simple scenario (temperature distribution resulting from a centered dipole magnetic field; pencil beaming) is not correct. Different hypotheses should be considered: the surface temperature distribution is possibly more complicated, e.g., as a consequence of a multipolar magnetic field; the hot spots may not be located close to the center of the hotter surface region; the emission beaming

function may have strong peaks at angles away from the normal to the surface element. We note that magnetospheric reprocessing of thermal photons (see previous sections) could possibly ease the problem. Such a mechanism would introduce phase delays between thermal spectral components, which would not be directly related to the properties of the surface but driven by the magnetospheric structure.

The observed phase-resolved behavior of the Three Musketeers does not seem to argue in favor of the simple, “canonical” picture of neutron stars as inclined, rotating, centered dipoles.

5. CONCLUSIONS

In general, the new X-ray phenomenology revealed by the *XMM-Newton* EPIC combination presents new aspects of these three isolated, local neutron stars. Rotating, polar hot spots are clearly detected for the first time. It is tempting to link their origin to energetic particle bombardment, following the Ruderman mechanism, especially because certainly two (and possibly all) of the Three Musketeers are strong γ -ray sources. In the case of Geminga, moreover, Caraveo et al. (2003) found genuine “smoking gun” evidence for this: the object’s bow shock is filled with electrons of just the right energy ($\sim 10^{14}$ eV) and luminosity (a few $\times 10^{28}$ ergs s^{-1}) to be the particles escaping from a polar cap.

However, the measurement of polar cap sizes, rendered accurate by the excellent distance measurements, does not match simple theoretical expectations. Three-dimensional geometry, beaming physics, as well as the role of magnetospheric scattering will have to be invoked for detailed models. The same holds true for the apparent sizes of the cool blackbody components. At least in one case they exceed the expected size of a standard neutron star. Simple atmospheric models worsen the problem.

However, before considering the implications of this finding on neutron stars equations of state, we must understand whether the parameters of the neutron star surfaces can be reliably derived from their thermal radiation or if some other mechanism is biasing our results.

Finally, the apparent puzzle posed by the difference in the phase alignments of the cool and hot components in the three objects is difficult to reconcile with existing pictures. This is reminiscent of the situation at γ -ray energies, at which apparently similar isolated neutron stars have markedly different light curves. It will be very interesting to look for contemporary X-ray and γ -ray data once *AGILE* and *GLAST* are in orbit with *XMM-Newton*.

We thank R. Manchester for his help with the Parkes radio ephemeris. We thank A. Possenti for his useful suggestions about radio timing data. We thank M. Conti and A. Pellizzoni for their help with the EGRET data. The *XMM-Newton* data analysis is supported by the Italian Space Agency (ASI). A. D. L. acknowledges an ASI fellowship.

REFERENCES

- Arons, J., & Scharlemann, E. T. 1979, *ApJ*, 231, 854
 Becker, W., & Aschenbach, B. M. 2002, *Neutron Stars, Pulsars, and Supernova Remnants*, ed. W. Becker, H. Lesch, & J. Trümper (Garching: MPE), 64
 Becker, W., & Trümper, J. 1997, *A&A*, 326, 682
 Becker, W., et al. 2004, *ApJ*, 615, 908
 Bertsch, D. L., et al. 1992, *Nature*, 357, 306
 Bignami, G. F., Caraveo, P. A., & Lamb, R. C. 1983, *ApJ*, 272, L9
 Bignami, G. F., Caraveo, P. A., Paul, J. A., Salotti, L., & Vigroux, L. 1987, *ApJ*, 319, 358
 Brisken, W. F., Thorsett, S. E., Golden, A., & Goss, W. M. 2003, *ApJ*, 593, L89
 Burwitz, V., et al. 2004, *Proc. SPIE*, 5165, 123
 Caraveo, P. A., Bignami, G. F., De Luca, A., Mereghetti, S., Pellizzoni, A., Mignani, R., Tur, A., & Becker, W. 2003, *Science*, 301, 1345
 Caraveo, P. A., Bignami, G. F., & Mereghetti, S. 1994, *ApJ*, 422, L87

- Caraveo, P. A., Bignami, G. F., Mignani, R. P., & Taff, L. 1996, *ApJ*, 461, L91
- Caraveo, P. A., De Luca, A., Mereghetti, S., Pellizzoni, A., & Bignami, G. F. 2004, *Science*, 305, 376
- Cheng, A. F., & Helfand, D. J. 1983, *ApJ*, 271, 271
- Cordova, F. A., Middleditch, J., Hjellming, R. M., & Mason, K. O. 1989, *ApJ*, 345, 451
- De Luca, A., & Molendi, S. 2004, *A&A*, 419, 837
- Everett, J. E., & Weisberg, J. M. 2001, *ApJ*, 553, 341
- Fierro, J. M., et al. 1993, *ApJ*, 413, L27
- Finley, J. P., Oegelman, H., & Kiziloglu, U. 1992, *ApJ*, 394, L21
- Greenstein, G., & Hartke, G. J. 1983, *ApJ*, 271, 283
- Greiveldinger, C., et al. 1996, *ApJ*, 465, L35
- Halpern, J. P., & Holt, S. S. 1992, *Nature*, 357, 222
- Halpern, J. P., & Ruderman, M. 1993, *ApJ*, 415, 286
- Halpern, J. P., & Wang, F. Y.-H. 1997, *ApJ*, 477, 905
- Harding, A. K., & Muslimov, A. G. 1998, *ApJ*, 500, 862
- . 2002, *ApJ*, 568, 862
- Jackson, M. S., Halpern, J. P., & Gotthelf, E. V. 2002, *ApJ*, 578, 935
- Kern, B., Martin, C., Mazin, B., & Halpern, J. P. 2003, *ApJ*, 597, 1049
- Kirsch, M., et al. (EPIC Calibration Team). 2004, EPIC Calibration Status, CAL-TN-0018-2-3 (Madrid: ESAC), http://xmm.vilspa.esa.es/external/xmm_sw_cal/calib/index.shtml
- Kramer, M., et al. 2003, *MNRAS*, 342, 1299
- Lattimer, J. M., & Prakash, M. 2001, *ApJ*, 550, 426
- Leahy, D. A. 1987, *A&A*, 180, 275
- Lyne, A. G., & Manchester, R. N. 1988, *MNRAS*, 234, 477
- Marshall, H. L., & Schulz, N. S. 2002, *ApJ*, 574, 377
- Mignani, R. P., Caraveo, P. A., & Bignami, G. F. 1997, *ApJ*, 474, L51
- Mignani, R. P., De Luca, A., & Caraveo, P. A. 2004, in *IAU Symp. 218, Young Neutron Stars and Their Environments*, ed. F. Camilo & B. M. Gaensler (San Francisco: ASP), 391
- Oegelman, H. 1995, *The Lives of the Neutron Stars*, ed. M. A. Alpar, U. Kiziloglu, & J. van Paradijs (Dordrecht: Kluwer)
- Oegelman, H., & Finley, J. P. 1993, *ApJ*, 413, L31
- Page, D. 1995, *ApJ*, 442, 273
- Pavlov, G. G., Zavlin, V. E., & Sanwal, D. 2002, *Neutron Stars, Pulsars, and Supernova Remnants*, ed. W. Becker, H. Lesch, & J. Trümper (Garching: MEP), 273
- Possenti, A., Mereghetti, S., & Colpi, M. 1996, *A&A*, 313, 565
- Psaltis, D., Oezel, F., & DeDeo, S. 2000, *ApJ*, 544, 390
- Ramanamurthy, P. V., Fichtel, C. E., Kniffen, D. A., Sreekumar, P., & Thompson, D. J. 1996, *ApJ*, 458, 755
- Rankin, J. M. 1993, *ApJS*, 85, 145
- Ruderman, M. 2004, *X-Ray and Gamma-Ray Astrophysics of Galactic Sources*, ed. M. Tavani, A. Pellizzoni, & S. Vercellone (Rome: ARACNE), 35
- Ruderman, M., & Sutherland, P. G. 1975, *ApJ*, 196, 51
- Strüder, L., et al. 2001, *A&A*, 365, L18
- Thompson, D. J., et al. 1999, *ApJ*, 516, 297
- Turner, M. J. L., et al. 2001, *A&A*, 365, L27
- Zavlin, V. E., & Pavlov, G. G. 2002, *Neutron Stars, Pulsars, and Supernova Remnants*, ed. W. Becker, H. Lesch, & J. Trümper (Garching: MEP), 263
- Zavlin, V. E., Pavlov, G. G., & Shibano, Y. A. 1996, *A&A*, 315, 141
- Zavlin, V. E., Shibano, Y. A., & Pavlov, G. G. 1995, *Astron. Lett.*, 21, 149